Evaluating MM_3 Multimodal Model Against High-Resolution Mapping for Earthquake-Induced Landslide Assessment in Kaikoura, New Zealand

Luis Angel Guerrero Hoyos

A thesis

submitted in partial fulfillment of the

requirements for the degree of

Master of Science in Civil Engineering

University of Washington

2025

Committee:

Joseph Wartman

Brett Maurer

Program Authorized to Offer Degree:

Civil and Environmental Engineering

University of Washington

Abstract

Evaluating MM_3 Multimodal Model Against High-Resolution Mapping for Earthquake-Induced Landslide Assessment in Kaikoura, New Zealand

Luis Angel Guerrero Hoyos

Chair of the Supervisory Committee:

Joseph Wartman

Department of Civil and Environmental Engineering

On November 14, 2016, New Zealand experienced an Mw 7.8 earthquake that triggered over 30,000 landslides. A high-resolution landslide inventory was developed within the study area, mapping 1,082 landslides. Approximately 48% of the inventory consisted of first-time failures, while approximately 52% were classified as reactivation failures. Landslides were categorized into two failure mechanisms: shallow and deep.

Geospatial data analysis and frequency ratio methods applied to the inventory revealed that topographic amplification factor (TAF), slope, geology, and normalized difference vegetation index (NDVI) are variables that strongly correlate with and significantly influence the occurrence of earthquake-induced landslides. A sensitivity analysis of the Multimodal Physics-Based Model (MM_3) showed that peak ground acceleration (PGA), friction angle, and cohesion

are the most influential variables for determining failure probability. The shallow model also demonstrated high sensitivity to soil depth.

MM_3 was then validated against high-resolution mapping to evaluate its predictive performance through more than 25,000 simulations. This evaluation resulted in a global model accuracy (area under the curve, AUC) of 0.82 and 0.79 for shallow and deep landslides, respectively.

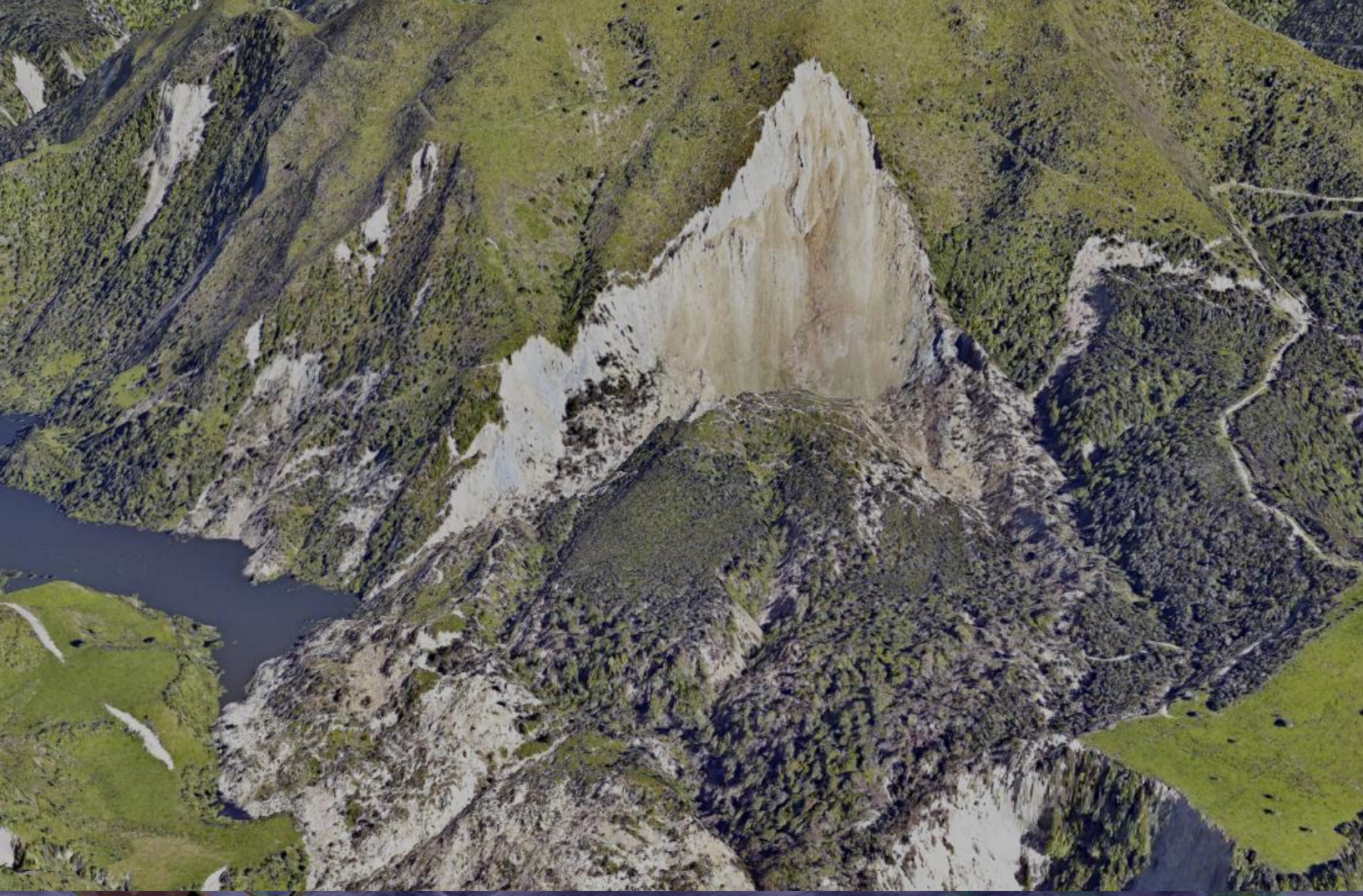

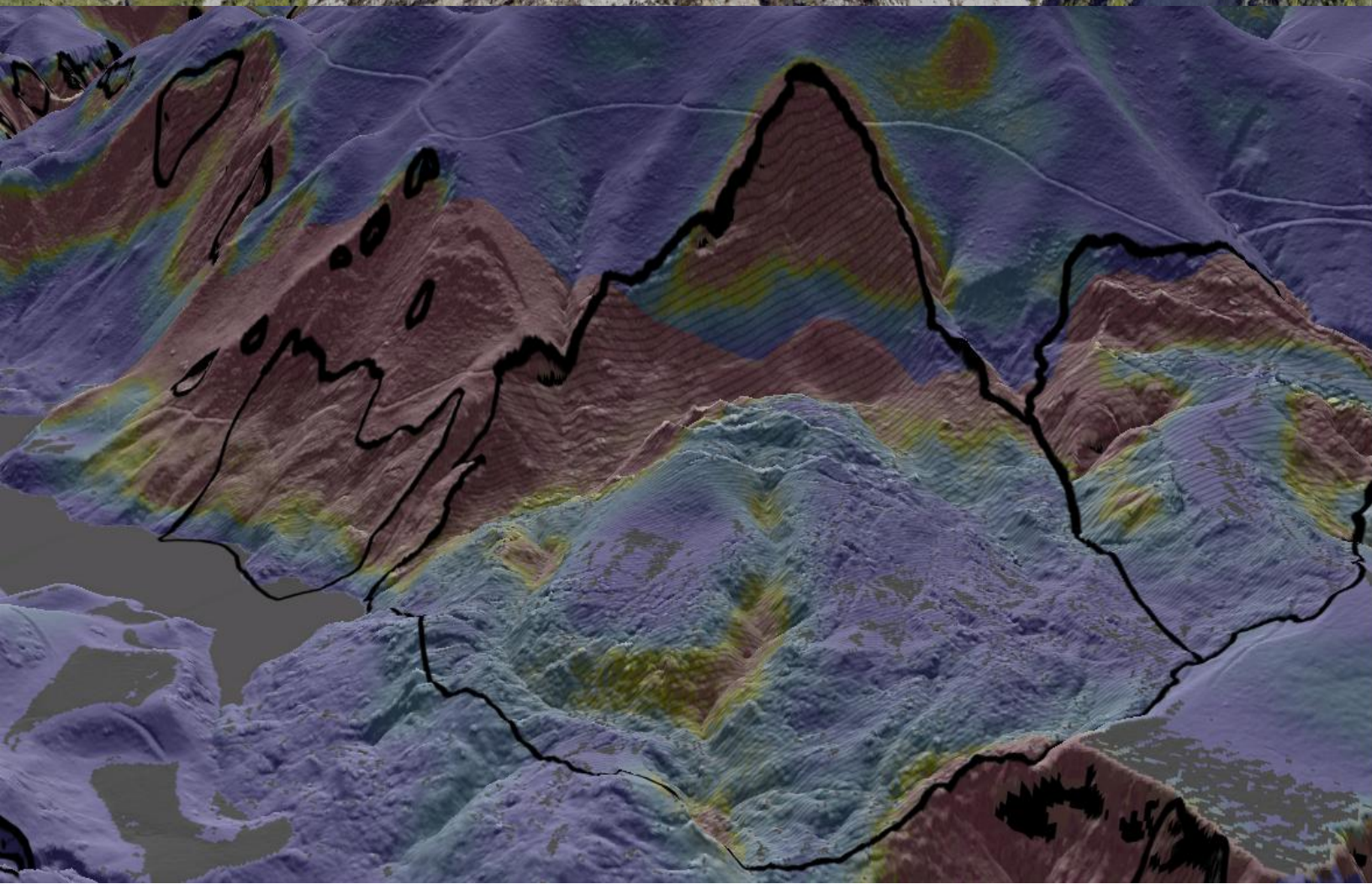

Acknowledgments

I would like to express my deepest gratitude to my advisor, Dr. Joseph Wartman, for his invaluable guidance, support, and encouragement throughout the course of my research and graduate studies. His mentorship has been instrumental in shaping my academic journey and professional development.

I am also grateful to the Civil and Environmental Engineering Department at the University of Washington, and to faculty members Dr. Brett Maurer, Dr. Pedro Arduino and Dr. Michael Gómez for their insightful feedback, instruction, and support during my time in the program. Special thanks also to GNS Science, Oregon State University, and the NHERI RAPID Facility for providing critical resources and data that contributed significantly to this work.

Finally, I am profoundly thankful for the unwavering love and support of my spouse, Diana Sanchez; my mother, Carmen Hoyos; my father, Benito Guerrero; and my siblings, Benito Guerrero Hoyos, Benito Guerrero Peinado, and Maria Guerrero. I would also like to thank my dear friend, Dajah Marie Mosley, and the rest of my friends whose encouragement has sustained me through every challenge and milestone along the way.

Table of Contents

List of Figures

List of Tables

List of Equations

1. Introduction

Earthquake-induced landslides can cause immediate and long-term economic losses, disrupt emergency rescue operations, and result in fatalities (A. R. R. Grant & Culhane, 2025). These landslides represent one of the most critical secondary hazards resulting from earthquake-induced ground shaking, significantly endangering lives, infrastructure, and property, especially in mountainous regions with high tectonic activity (Dahal et al., 2023). To address these hazards, reliably identifying regions susceptible to earthquake-induced landslides is essential for effective emergency management and strategic community planning (Lombardo & Tanyas, 2022).

Landslide inventories serve as a preliminary step toward landslide susceptibility, hazard, and risk assessment (van Westen et al., 2008), revealing the distribution, types, and patterns of landslides in relation to morphological and geological characteristics (GUZZETTI et al., 1996). The availability of new remote sensing technologies for landslide detection and mapping facilitates the production of landslide maps and enables the definition of criteria to evaluate their quality (Guzzetti et al., 2012).

This research aims to advance earthquake-induced landslide hazard assessment by addressing two interrelated challenges. First, it seeks to improve understanding of landslide behavior by mapping detailed landslide characteristics, particularly distinguishing between first-time failures and reactivations. Identifying these differences is essential for unraveling the physical processes that govern slope instability and for informing targeted mitigation strategies. Second, this study focuses on improving a regional-scale physics-based model for predicting landslide occurrence, with the goal of supporting more effective early warning systems and risk management efforts. By leveraging geospatial data and remote sensing technologies, these

models can provide timely, spatially explicit insights into landslide susceptibility over broad areas.

2. Study Area and Earthquake

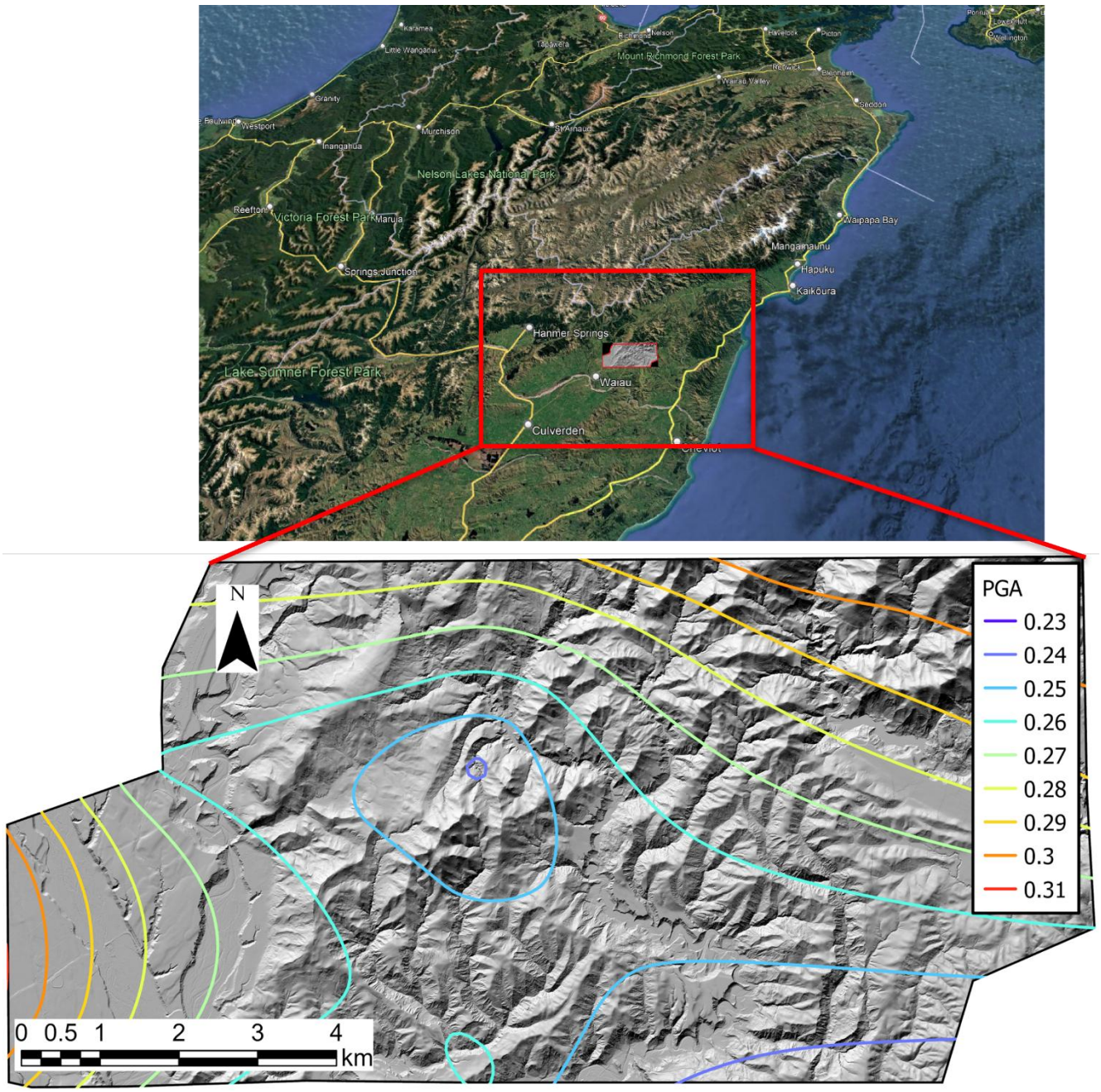

Figure 1. Area of Interest in South Island, New Zealand. PGA model by Bradley (2017).

The study area is located in North Canterbury on New Zealand's South Island (Figure 1), covering approximately 82 km². The site is situated ~4 km and ~8 km northeast of Waiau and the earthquake epicenter, respectively (Dessington, 2020), and lies along the southwest-northeast rupture propagation path from the earthquake epicenter (Kaiser et al., 2017). The diverse landforms within the area make it ideal for understanding the distribution of landslides triggered by the 14 November 2016 Kaikoura earthquake.

The 14 November 2016 Kaikoura earthquake had a moment magnitude (Mw) of 7.8 and occurred at 12:03 a.m. local time (Kaiser et al., 2017). Ground motion peak ground acceleration (PGA) models developed for the study area following Bradley et al. (2017) show that PGA ranges between 0.23g and 0.31g within the study area, as observed in Figure 1. Multiple efforts have contributed to the development of a comprehensive coseismic landslide inventory for the Kaikoura earthquake. The inventory has progressed through three versions: Version 1.0 included 10,195 large landslides mapped as points; Version 2.0 expanded to 29,557 source areas, also as points. This study presents Version 3.0, the first polygon-based release, with 31,623 source areas and 26,559 debris trails (Jones et al., 2025).

3. Landslide Inventory

An initial landslide inventory was developed by Massey et al. (2018) and subsequently enhanced by Pollock et al. (2020), resulting in a total of 561 mapped landslides within the study area. A first contribution of this thesis research is the addition of 521 landslides to the existing (Pollock et al., 2020) inventory.

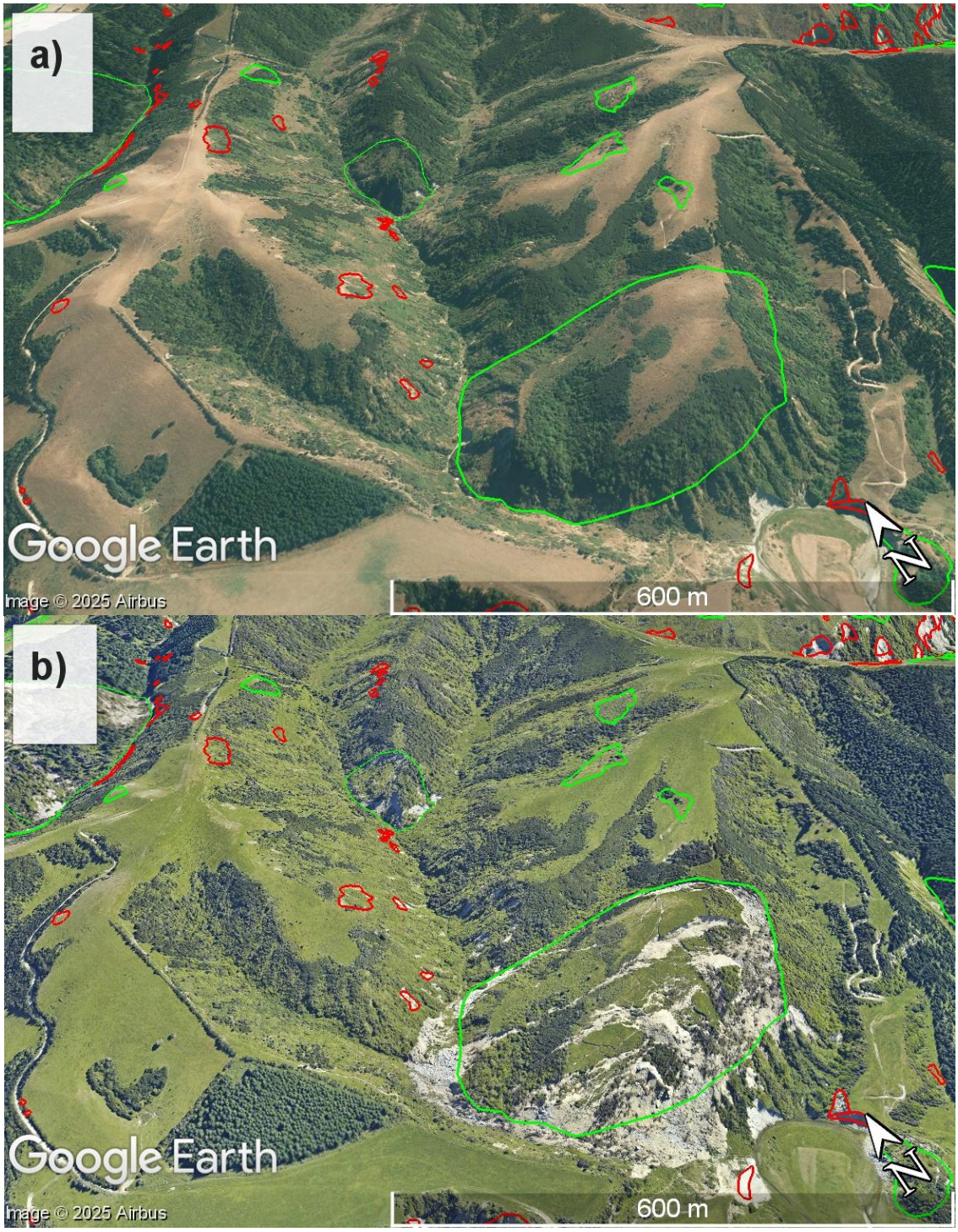

Figure 2. Satellite image a) before and b) after the earthquake. Mapped landslides in green (deep) and red (shallow).

3.1. Database Creation

High-resolution post-earthquake LiDAR data, openly available in Land Information New Zealand (LINZ) databases, was utilized to map landslides. Additionally, temporal satellite imagery and orthomosaics were instrumental in distinguishing between first-time failures and reactivations. Crack mapping developed by Dessington (2020) played a critical role in inventory development, particularly for areas where failure was not characterized by large displacements.

Landslides were classified using the updated Varnes landslide classification system following Hungr et al. (2014), then divided into two groups: shallow and deep failures. This classification approach aligns with the physics-based model requirements described later in this document. Figure 2 shows pre- and post-earthquake snapshots within the study area, with deep slides shown in green and shallow slides in red.

Landslide activation characteristics were also mapped, distinguishing between first-time failures and reactivations. The criteria implemented for this differentiation are detailed in Table 1.

Table 1. Judgement summary on defining activation characteristics of landslides.

	Deep	**Shallow**
Reactivation	Ancient scarps or deposits that moved during the EQ	Denuded areas with signs of previous landslide activity
First-Time	New scarps that extend beyond ancient scarps	Vegetated areas without signs of previous landslide activity

Figure 3 presents the quantification of newly added landslides and final inventory statistics. The 521 new landslides comprise 76 deep slides and 445 shallow slides. The complete inventory contains 399 shallow first-time failures, 542 shallow reactivations, 121 deep first-time failures, and 20 deep reactivations, totaling 1,082 landslides in the updated database.

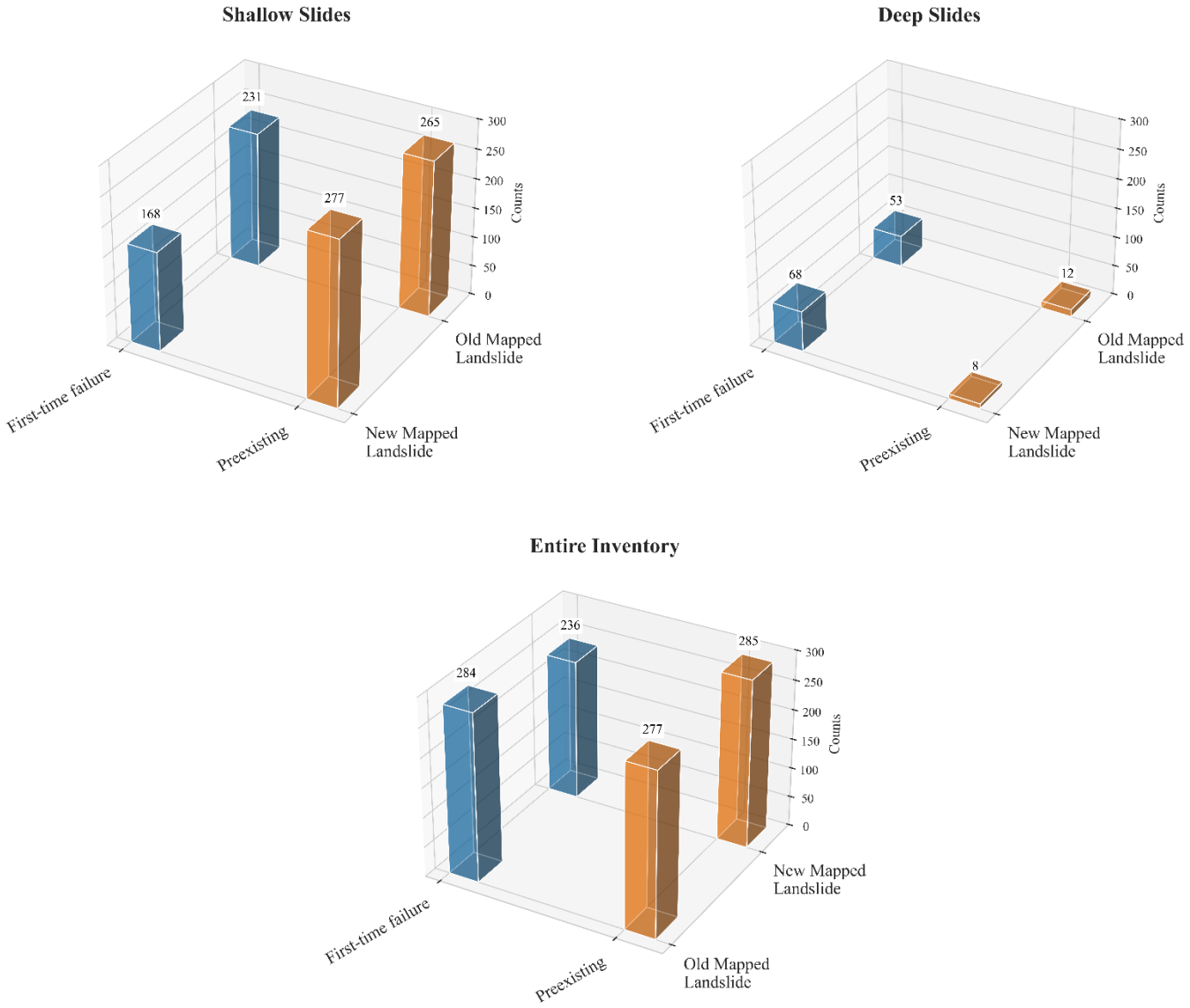

Figure 3. Quantification of newly added landslides in the inventory.

Landslide size statistics can be analyzed using cumulative or non-cumulative size distributions, typically represented by frequency-area distribution (FAD) curves plotted for landslide-area bins versus corresponding non-cumulative frequency-density values (Tanyaş et al., 2018). Two features control FAD shape: a power-law distribution for medium to large landslides, and a divergence from the power-law toward high frequencies with a rollover point where frequencies decrease for smaller landslides. The point where the FAD diverges from the power-law is defined as the cutoff point (Guzzetti et al., 2002; Stark & Hovius, 2001).

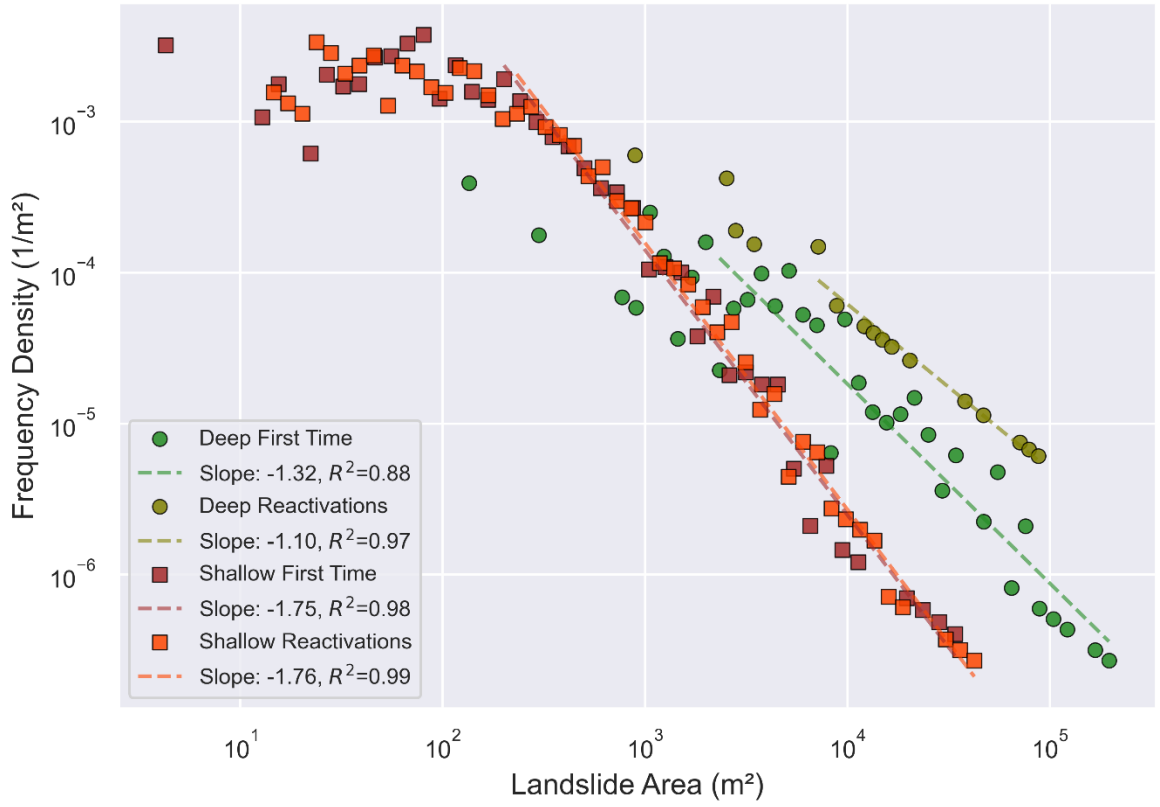

Figure 4. Area magnitude vs Frequency Density curves for the 4 different modes and activations.

Figure 4 presents FAD curves for the four landslide types mapped in this study. Landslide size distribution analysis suggests that shallow slides are dominated by small events, with most having surface areas between 200 m^2 and 700 m^2 (cutoff point), and no significant distinction between shallow first-time failures and reactivations. Conversely, deep landslides tend to be larger with fewer small events, and reactivations are slightly larger than first-time failures, as evidenced by the shift between deep and shallow curves. Specifically, the cutoff point for deep reactivations is approximately 9,000 m^2 compared to 5,000 m^2 for deep first-time failures.

3.2. Geospatial Data Analysis

Various methods and techniques have been proposed for landslide susceptibility mapping, including frequency ratio (FR), statistical index (SI), weights of evidence (WoE), logistic regression, and multivariate regression (Razavizadeh et al., 2017). This study adopted FR to identify morphometric characteristics that favor earthquake-induced landslide occurrence.

FR considers the impact of each conditioning factor on landsliding and assigns weights precisely (Lee & Pradhan, 2007). Weights greater than 1 indicate stronger correlation, while weights less than 1 represent weaker correlation (Lee & Min, 2001). The frequency ratio calculation follows Equation 1 (Jaafari et al., 2014; Regmi et al., 2014):

$$FR = \frac{N_{pix}(SX_i) \Big/ \sum_{i=1}^{m} SX_i}{N_{pix}(X_j) \Big/ \sum_{j=1}^{n} N_{pix}(X_j)} = \frac{E/F}{M/L} \qquad \textit{Equation 1}$$

Where E is the number of pixels with landslides in a specific class within the area of interest, F is the total number of pixels with landslides within the area of interest, M is the number of pixels in the specific class within the area of interest, and L is the total pixels in the entire area of interest.

Terrain variables analyzed include slope, topographic amplification factor, normalized difference vegetation index (NDVI), geology, distance to faults, landforms, and curvature. Each variable is described below, with all variables sampled using median values as the representative statistic.

3.2.1. Slope

Slope angle is a key conditioning factor influencing slope stability (Varnes, 1984). Figure 5 illustrates (a) the slope map overlaid with the landslide inventory (in black), and (b–c) the statistical distribution of median slope angles within both the study area and landslide areas.

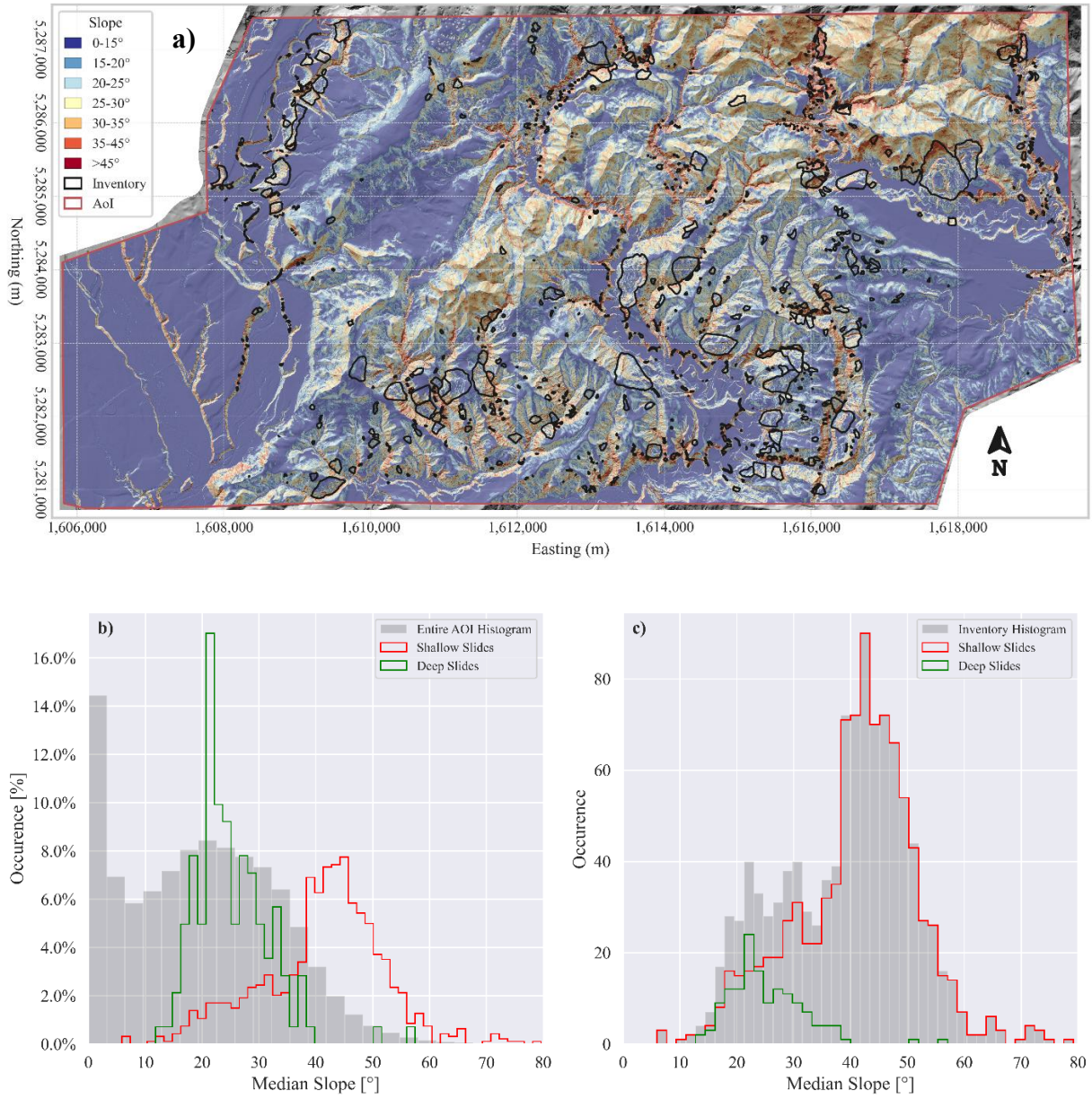

Figure 5. a) Slope map for the study area (AoI), landslides in black. b) Slope statistic distribution as percentage in gray for entire AoI and sampled median slope for shallow slides in red and deep slides in green. c) Slope statistic distribution as counts in gray for landslide areas and sampled median slope for shallow slides in red and deep slides in green.

Slope was divided into seven classes (Figure 5a): 0°-15°, 15°-20°, 20°-25°, 25°-30°, 30°-35°, 35°-45°, and >45°. Figure 5b and Figure 5c shows the distribution of median slope values for both shallow slides in red and deep slides in green. Figure 5b displays data as percentages compared against the entire study area distribution (gray), while Figure 5b compares mode distributions against landslide areas only as frequency counts.

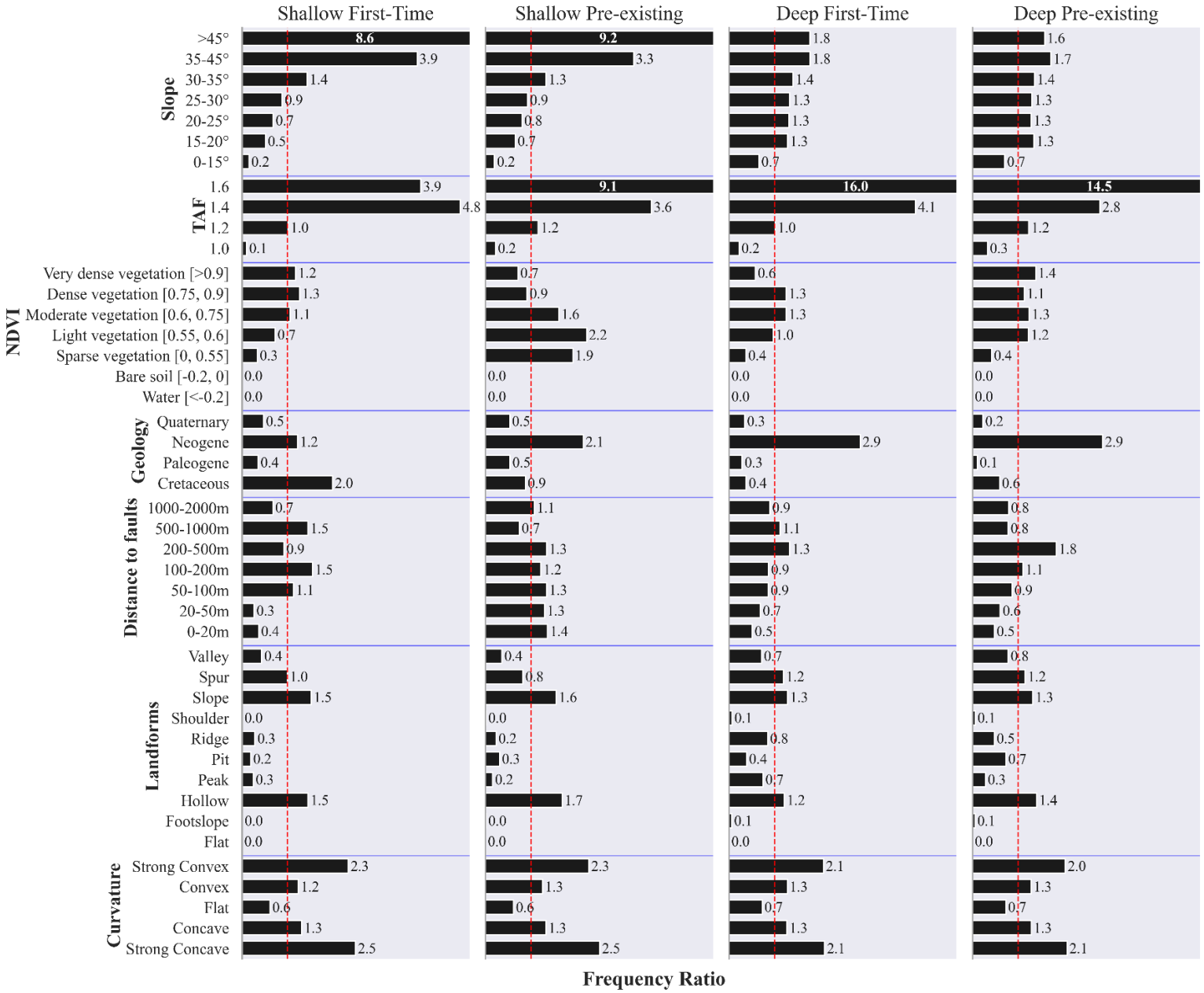

Figure 6. Frequency ratio results for the considered variables.

Significant differences exist between slope preferences for different failure modes: shallow slides preferentially occur on slopes ranging from 40° to 50°, whereas deep slides follow the slope distribution of the entire study area, with most occurring on slopes ranging from 20° to 30°. FR results (Figure 6) show that steeper slopes (>35°) strongly correlate with shallow earthquake-induced landslide occurrences, while no single class stands out for deep earthquake-induced landslides, though slopes steeper than 15° correlate with these occurrences.

3.2.2. Topographic Amplification Factor (TAF)

Studies support the hypothesis that ground motions can be amplified based on near-surface impedance contrasts (local deposits or highly fractured rocks) (Moore et al., 2011) and position within the slope (near ridge crests or slope breaks) (Kaiser et al., 2014). This research adopts the topographic amplification factor map from Eurocode 8 as described by Massey et al. (2023) and displayed in Figure 6b. While determining TAF can be challenging due to complex contributing factors requiring interpretation and expert judgment, the criteria suggested by Massey et al. (2023) include:

- Slopes < 15° → **TAF = 1.0**
- 10m (r=37m) < LSR < 30m (r=17m) and 15° < Slopes < 30° → **TAF = 1.2**
- LSR > 30m (r=52m) and Slopes > 30° → **TAF = 1.4.**
- Combine these 3 and add **TAF=0.2** for those classified as soils and/or fractured rocks.

Where LSR represents Local Slope Relief, defined as the difference in elevation between a pixel and the lowest-elevation pixel within a search radius (r), essentially the height of the pixel within a given slope. Figure 7a exhibits the TAF map for the study area with the four different classes and the landslide inventory in black.

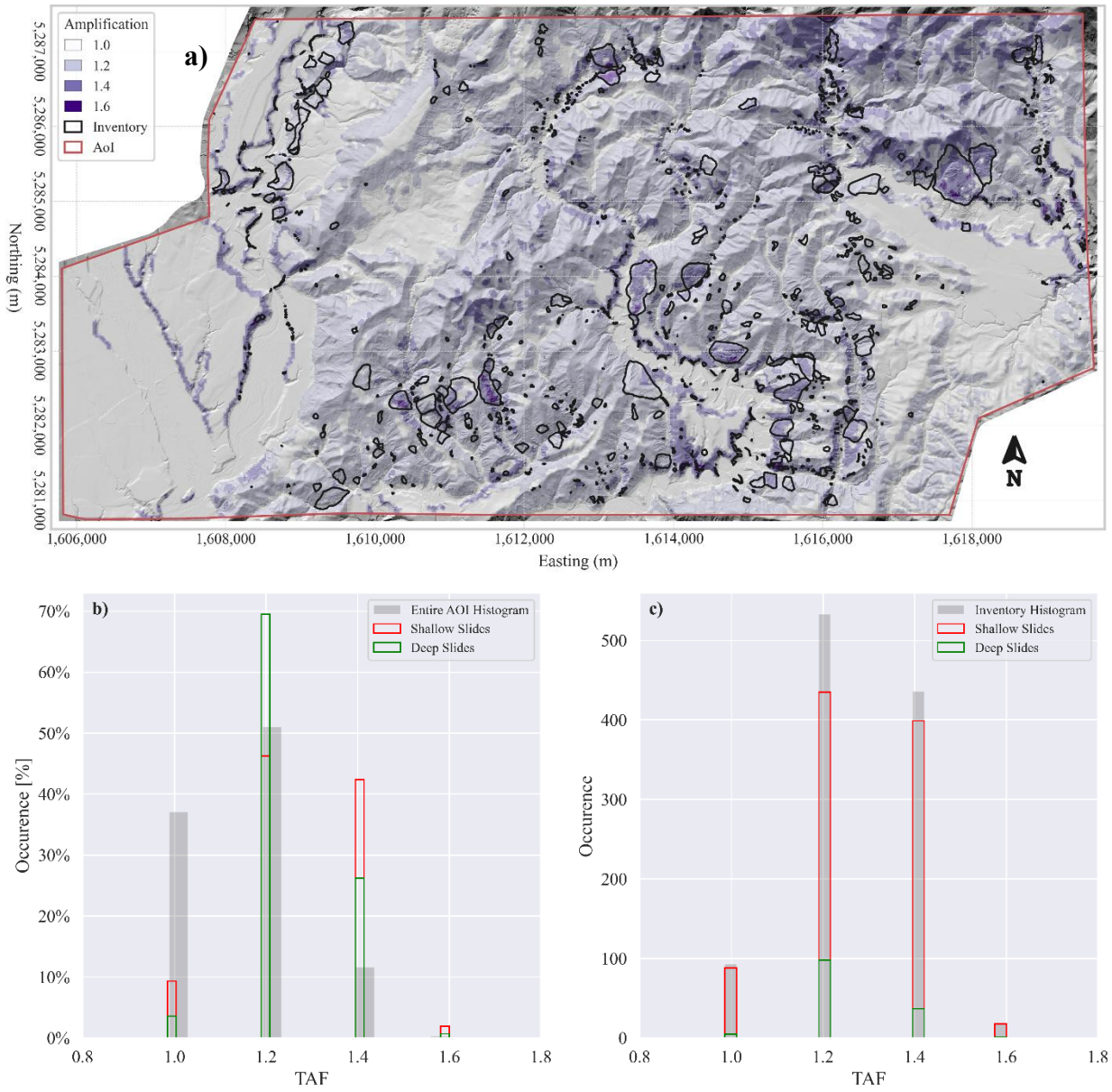

Figure 7. a) Topographic Amplification Factor (TAF) map for the study area (AoI), landslides in black. b) TAF statistic distribution as percentage in gray for entire AoI and sampled median TAF for shallow slides in red and deep slides in green. c) TAF statistic distribution as counts in gray for landslide areas and sampled median TAF for shallow slides in red and deep slides in green.

The FR results for TAF in Figure 6 indicate that values of 1.4 and 1.6 are strongly correlated with the occurrence of both deep and shallow earthquake-induced landslides. Additionally, Figure 7b shows that a higher percentage of shallow landslides occur near ridges ($1.4 < TAF < 1.6$) compared to deep landslides ($TAF = 1.2$).

3.2.3. Normalized Difference Vegetation Index (NDVI)

NDVI is a widely used metric for quantifying vegetation health and density using sensor data. Vegetation health and density can be interpreted as a contribution to root cohesion. NDVI is calculated from satellite imagery using the satellite's spectrometer or radiometric sensor, which measures and stores reflectance values for both red and near-infrared (NIR) bands on separate channels or images. Kriegler et al. (1969) first proposed NDVI, which is calculated by subtracting the red channel from the near-infrared (NIR) channel and dividing their difference by the sum of the two channels, as expressed mathematically in Equation 2:

$$NDVI = \frac{NIR - Red}{NIR + Red} \qquad \textit{Equation 2}$$

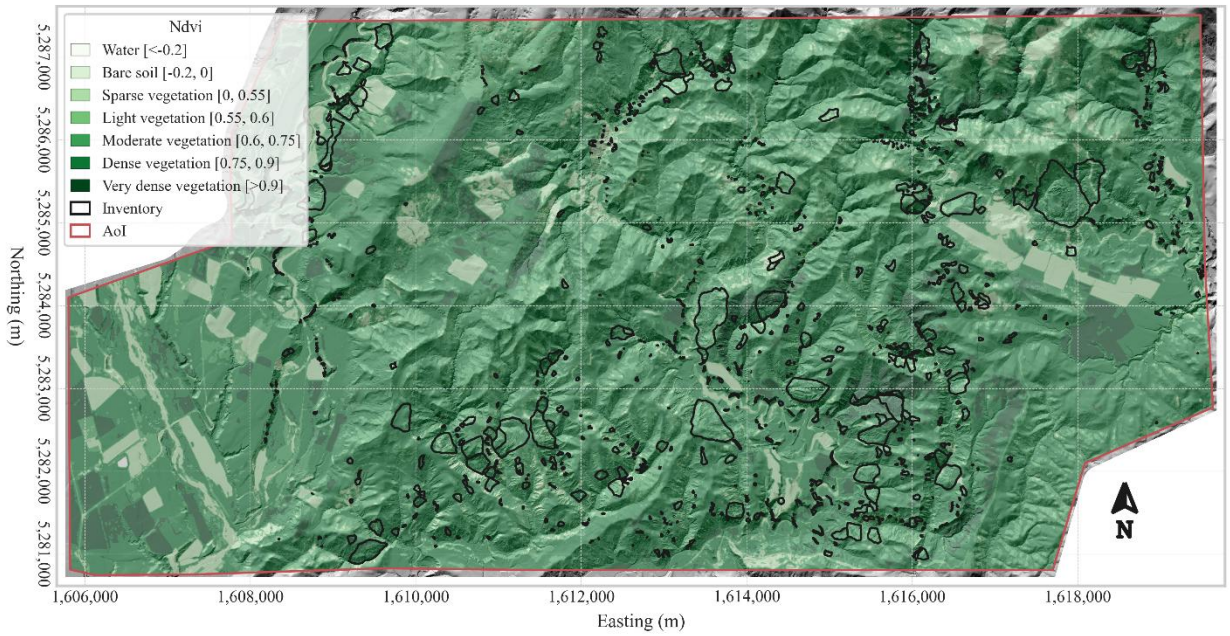

Figure 8. a) Normalized Difference Vegetation Index (NDVI) map for the study area (AoI), landslides in black.

In this study, NDVI values were classified into seven intervals, as depicted in Figure 8: NDVI < -0.2 corresponds to water pixels; values between -0.2 and 0 represent bare soil; 0 to 0.55 indicates sparse vegetation; and ranges of 0.55–0.6, 0.6–0.75, 0.75–0.9, and >0.9 represent light, moderate, dense, and very dense vegetation, respectively.

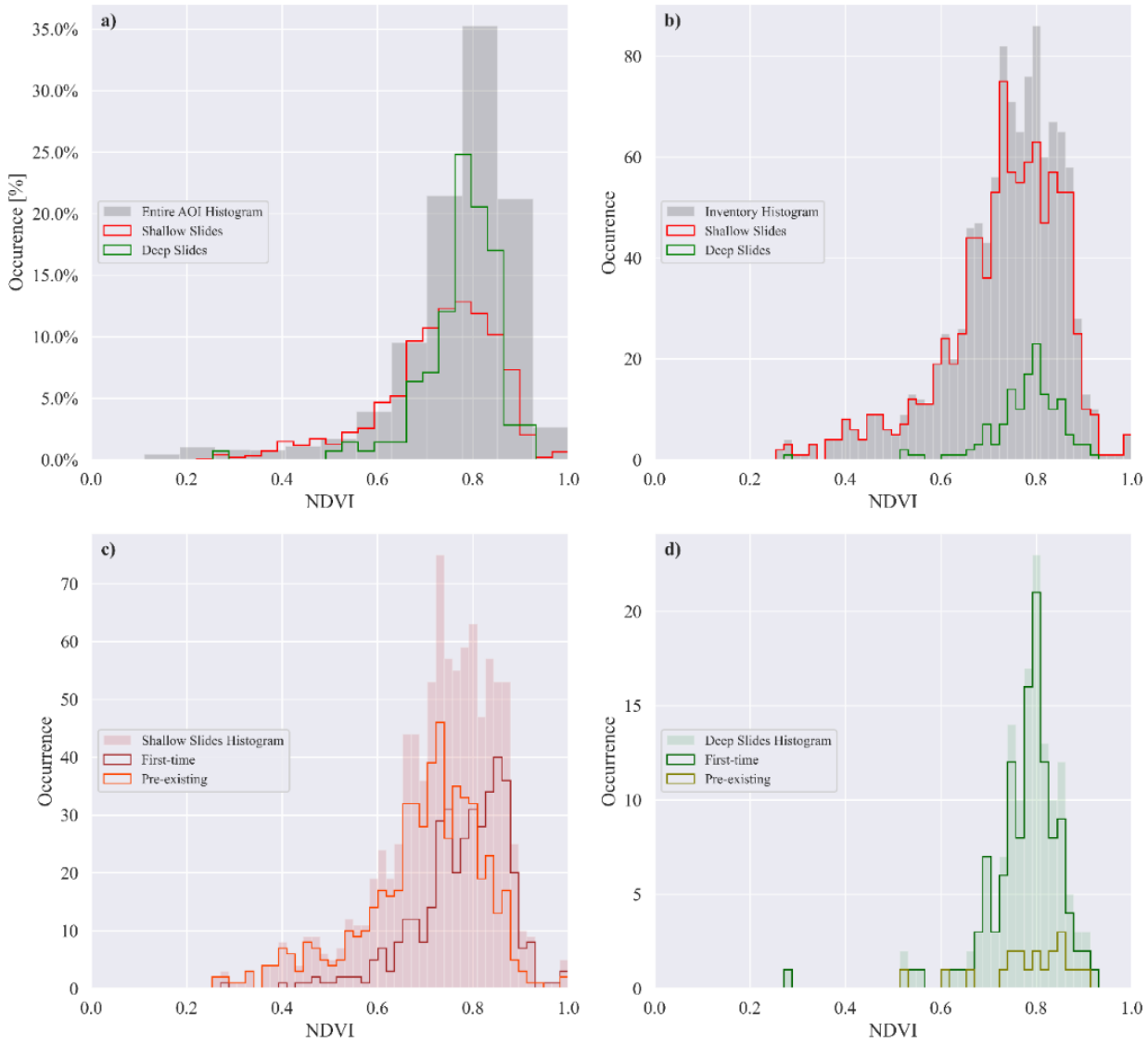

Figure 9. a) Normalized Difference Vegetation Index (NDVI) statistic distribution as percentage in gray for entire AoI and sampled median slope for shallow slides in red and deep slides in green. b) NDVI statistic distribution as counts in gray for landslide areas and sampled median slope for shallow slides in red and deep slides in green. c) NDVI statistic distribution as counts in red for shallow landslide areas and sampled median slope for shallow first-time slides in brown and shallow reactivations slides in orange. d) NDVI statistic distribution as counts in green for deep landslide areas and sampled median slope for deep first-time slides in dark green and deep reactivations slides in olive.

FR results for NDVI in Figure 6 reveal a significant distinction between areas susceptible to first-time shallow landslides and those prone to shallow reactivations. Lower NDVI values, indicative of sparse vegetation, are more strongly associated with initial failures, suggesting that vegetation cover plays a stabilizing role. In contrast, for deeper landslides, NDVI does not appear to be a discriminating factor when values exceed 0.55, indicating that beyond a certain vegetation threshold, NDVI loses its predictive power for distinguishing between first-time and reactivated deep-seated failures.

Figure 9c shows a slight overall difference in NDVI distribution between shallow and deep landslides, with deeper landslides generally occurring in areas with higher NDVI values. Notably, NDVI ranges can differentiate between shallow landslide types: first-time failures tend to cluster within higher NDVI values (0.8–0.9), while shallow reactivations are more common in moderately vegetated areas (NDVI 0.65–0.8), reinforcing NDVI's potential as an indicator of slope failure behavior.

3.2.4. Geology

Geological materials exhibit a wide range of geotechnical properties, including cohesion, internal friction angle, and unit weight, based on factors such as mineralogical composition, degree of weathering, age, and diagenetic history. These variations influence the mechanical behavior and shear strength of materials, thereby affecting slope stability and landslide occurrence likelihood. Understanding these differences is essential for accurately assessing landslide susceptibility across different geologic units.

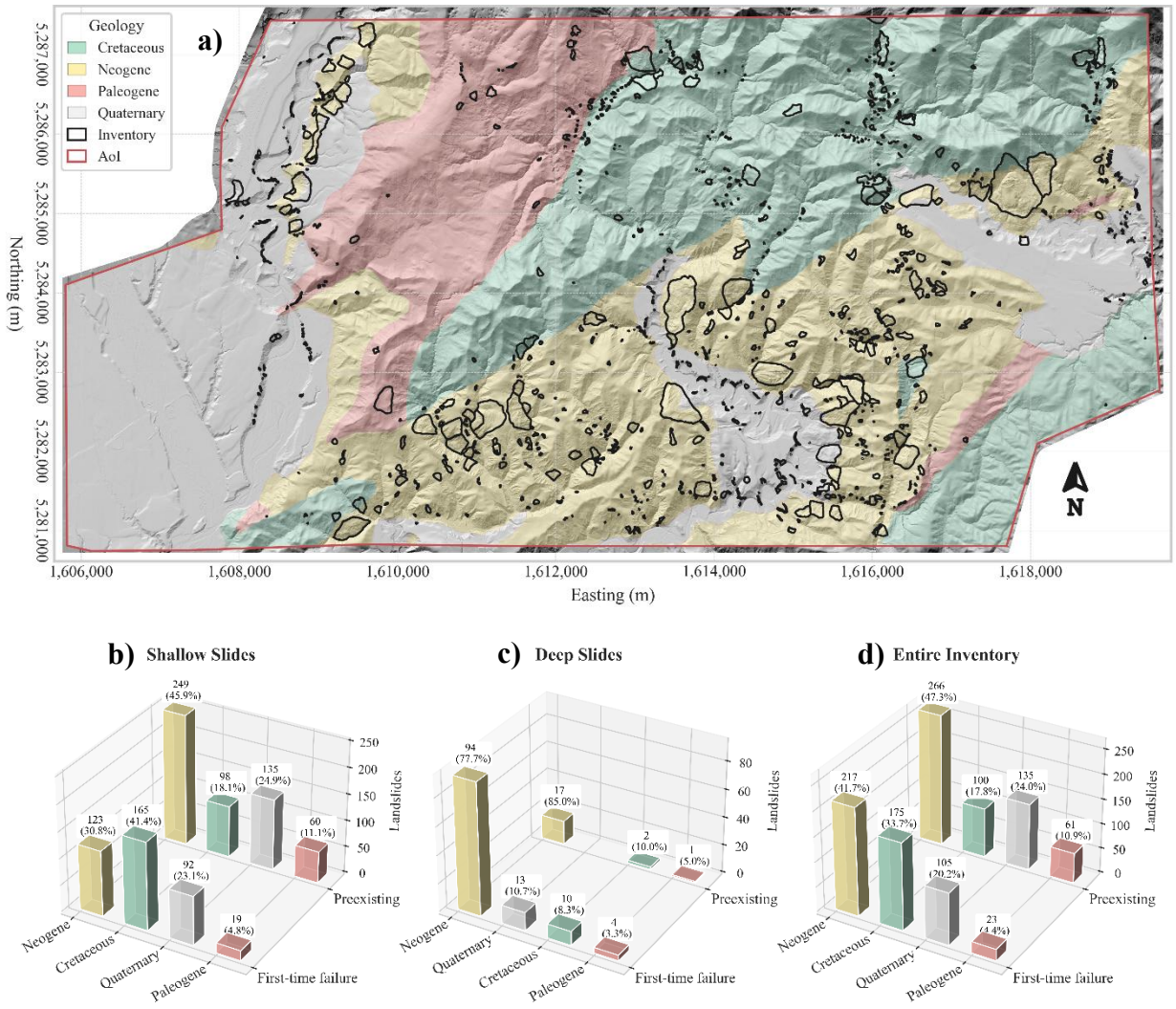

Figure 10. a) Geology map for the study area (AoI), landslides in black. b) Shallow landslides distribution by geology and activation characteristics. c) Deep landslides distribution by geology and activation characteristics. C) Entire landslides mapped distribution by geology and activation characteristics.

Geologic data from the Institute of Geological and Nuclear Sciences (GNS, 2020) at a scale of 1:250,000 indicates that the study area comprises four main geologic units, as shown in Figure 6d. As described by Massey et al. (2018), these units include: Quaternary alluvial deposits, consisting primarily of sands, silts, and gravels; Paleogene limestones, which are typically slightly weak, massive rocks; Neogene siltstones and limestones, characterized as fine-

grained and generally weak; and Cretaceous sandstones and argillites, commonly referred to as graywackes, which are considered strong rocks. These lithological differences imply a range of geotechnical behaviors that can significantly influence slope stability and landslide susceptibility across the region.

FR results further highlight the influence of geological materials on landslide occurrence. As shown in Figure 6, Neogene siltstones exhibit a strong correlation with all types of landslides, suggesting that their weak, fine-grained nature contributes to slope instability regardless of failure type. In contrast, Figure 10b reveals that Cretaceous sandstones and argillites are strongly associated with shallow first-time failures, indicating that despite their generally strong geotechnical properties, certain conditions within these units, such as intense fracturing or steep slopes, may promote the initiation of new shallow slope failures. These results underscore the importance of considering lithological variability when evaluating landslide susceptibility.

3.2.5. Distance to Faults

Distance to faults was calculated for every pixel in the study area as the shortest distance to the nearest mapped fault trace. Fault data were obtained from Langridge et al., (2016), providing a comprehensive representation of active and potentially active fault structures. The continuous distance values were categorized into eight classes: 0–20 m, 20–50 m, 50–100 m, 100–200 m, 200–500 m, 500–1,000 m, 1,000–2,000 m, and greater than 2,000 m, as shown in Figure 11a. This classification enables analysis of how proximity to faults influences landslide occurrence, capturing both near-fault effects and broader spatial patterns of fault-related slope instability.

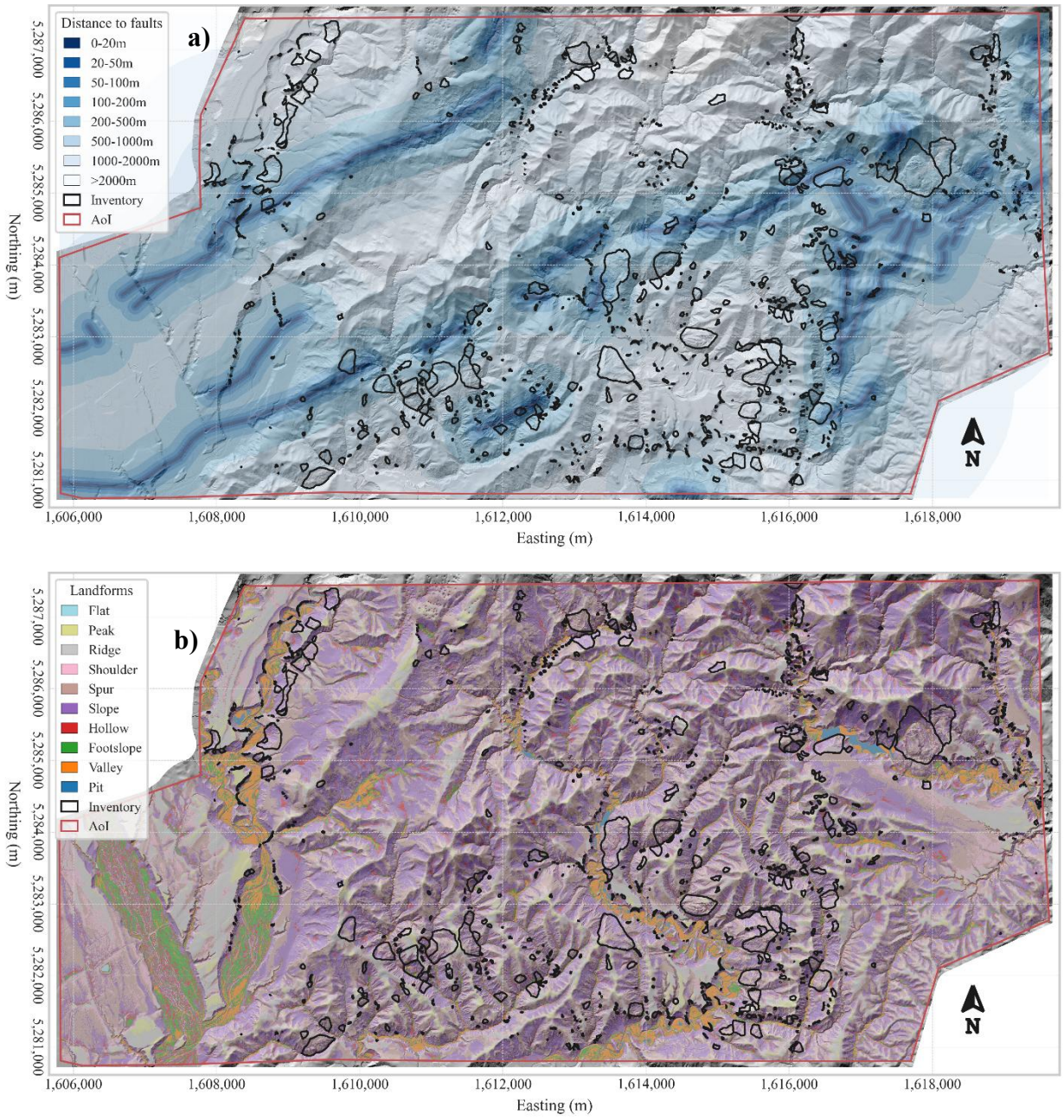

Figure 11. a) Distance to faults map for the study area (AoI), landslides in black. b) Landforms map for the study area (AoI), landslides in black.

FR results in Figure 6 reveal that distances to faults in the range of 200–500 m are notably correlated with deep-seated landslide occurrence. This suggests that deep failures may be influenced by broader fault-related deformation zones or stress fields rather than immediate

proximity to the fault trace. In contrast, no significant distinction is observed among distance classes for shallow landslides, indicating that shallow failures are less sensitive to fault proximity or may be driven by more localized surface conditions such as slope angles, vegetation cover, or material properties.

3.2.6. Landforms

Figure 12 presents the landform classification, derived using the built-in Geomorphon tool in ArcGIS Pro based on the method developed by Jasiewicz & Stepinski (2013). This approach categorizes the landscape into ten distinct geomorphological forms, such as ridges, valleys, slopes, and flats, based on local terrain patterns and the spatial arrangement of elevation values.

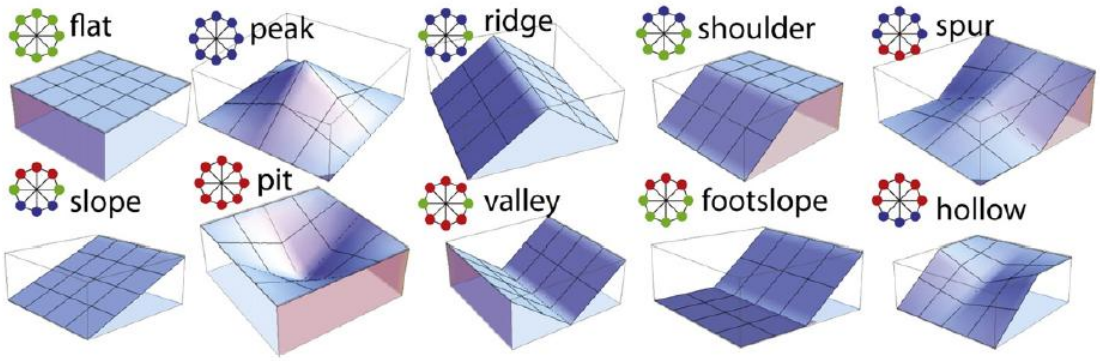

Figure 12. Landforms after Jasiewicz & Stepinski (2013).

The landforms map is presented in figure 11b and frequency ratio (FR) results in Figure 6 show that spurs are particularly associated with deep-seated landslides, likely due to their topographic prominence and structural control, which can favor the development of deeper failure planes. In contrast, slopes and hollows correlate with both shallow and deep landslides, reflecting their inherent geomorphic characteristics that contribute to instability across different landslide types.

3.2.7. Curvature

Curvature was calculated using the second derivative of the elevation surface through a built-in function in ArcGIS Pro, resulting in values that typically range between -0.5 and 0.5. These values were classified into five distinct classes to facilitate analysis as it is observed in Figure 13. However, as shown in Figure 6, curvature does not exhibit meaningful correlation with landslide occurrence, at least not at the pixel level. This suggests that curvature alone may not be a reliable predictor of slope failure in this study area, possibly due to its sensitivity to the evaluation scale.

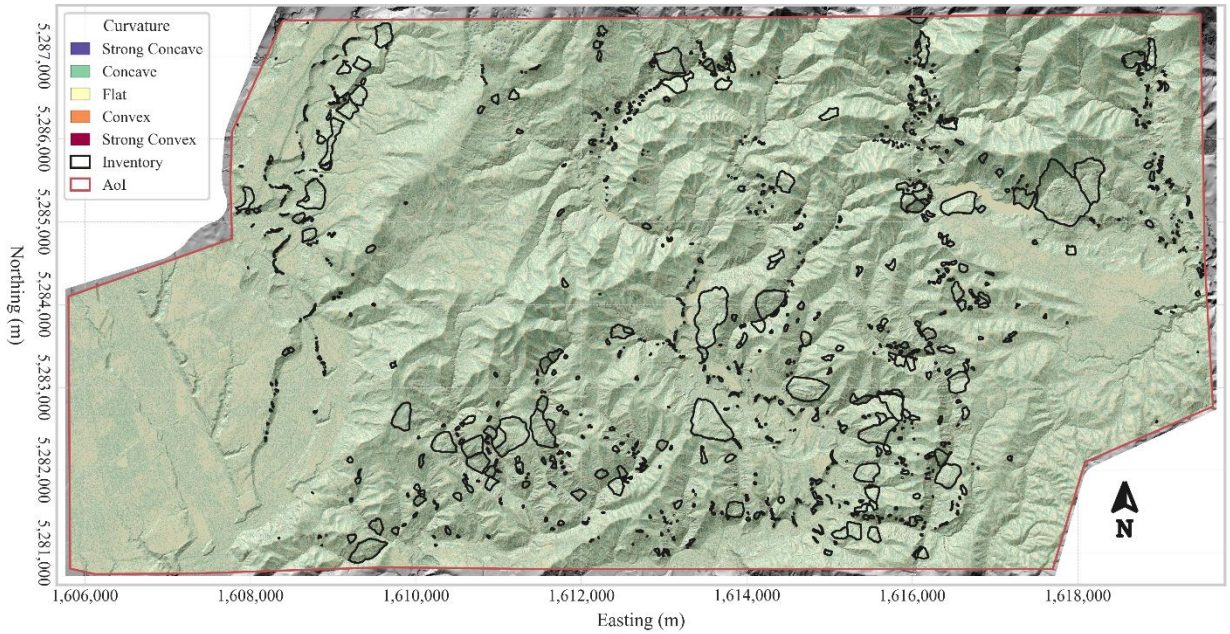

Figure 13. Curvature map for the study area (AoI), landslides in black.

3.3. Interpretation

The updated landslide inventory and geospatial analysis offer a comprehensive view of the conditions that governed slope failures during the 2016 Kaikoura earthquake for the study area. This synthesis highlights the interactions between landslide mechanisms, landscape characteristics, and seismic forces, providing the empirical foundation for validating the physics-based MM_3 model further in Section 4. The dominance of shallow landslides, accounting for over 80% of mapped events, immediately stands out, with reactivations occurring at similar frequencies to first-time failures. This prevalence aligns with the expectation that shallow, weak, and loose soils on steep slopes are especially vulnerable during strong shaking. Interestingly, while shallow landslides were small (typically 200–700 m^2), deep landslides were significantly larger, particularly when reactivated. This scaling behavior reflects fundamentally different mobilization processes, as smaller masses are inherently easier to displace than larger ones and suggests that preconditioning plays a key role in governing failure mode.

The geospatial analysis reinforces this mechanical dichotomy. Shallow failures clustered on steep slopes (40°–50°), consistent with global coseismic landslide patterns (e.g., Dahal et al., 2023) and showed strong associations with topographic amplification (TAF > 1.4), echoing the ridge-top amplification effects documented by Kaiser et al. (2014). NDVI further revealed that first-time shallow failures were concentrated in densely vegetated areas (NDVI 0.8–0.9), while reactivations were more common in areas with moderate vegetation cover (NDVI 0.65–0.8), likely reflecting vegetation loss from prior events. This aligns with the stabilizing influence of vegetation on slope stability reported by Grant et al. (2016).

In contrast, deep failures concentrated on more moderate slopes (20°–30°), showing little sensitivity to vegetation. This pattern points to fundamentally different controls on slope

instability. These failures are likely governed by subsurface structural weaknesses, such as bedding planes, foliation, or jointing, coupled with elevated pore pressures and seismic stress redistribution. Unlike shallow failures, which are closely linked to surface steepness and vegetation, deep failures emerge from subsurface-dominated processes that allow instability even on gently inclined terrain.

The role of geology also plays a crucial part in understanding why landslides failed where they did, acting as a key control on slope stability. Weak, fine-grained Neogene rocks were strongly associated with all landslide types, as expected given their low shear strengths. Yet a surprising pattern emerged: shallow first-time failures were also common in areas dominated by Cretaceous sandstone, rocks typically considered strong and competent. This unexpected relationship suggests additional controls such as weathering, or topographic focusing of seismic energy. Notably, weathered sandstones can degrade into loose, cohesionless sands that are highly susceptible to shallow sliding when saturated or shaken. Because these loose sands lack internal cohesion, they are more prone to fail in small, shallow slides rather than deeper, coherent mass movements. This reaffirms the importance of closer structural and geotechnical scrutiny to capture in-situ rock weakening and material heterogeneity, factors often overlooked when relying solely on surface geology maps. To reduce uncertainty in material strength assumptions, especially in areas with complex or weathered lithologies, site-specific subsurface investigations are essential. Techniques such as exploration borings, geophysical surveys, and laboratory testing provide critical data to constrain input parameters for modeling and improve the reliability of landslide hazard assessments.

These findings carry important implications for the development and application of the MM_3 framework. The distinct patterns observed between shallow and deep-seated landslides

underscore the necessity of a multimodal modeling approach. For shallow failures, the strong influence of steep slopes, NDVI (as a proxy for vegetation and root strength), and surficial conditions indicate that models must prioritize surface metrics such as slope angle, vegetation-derived reinforcement, and spatial variability in soil thickness. In contrast, deep failures are more strongly governed by subsurface factors, including lithology, geological structures (e.g., bedding planes and fractures), and seismic stress redistribution, necessitating a deeper geotechnical and structural characterization of the terrain. Additionally, the influence of ground motion amplification and spatial heterogeneity in seismic energy further supports the need to represent shaking incoherence in model inputs. The updated inventory thus serves not only as a high-resolution benchmark for MM_3 validation, but also as a diagnostic tool to refine its input parameters.

4. Physics-Based Model

Traditional regional-scale landslide hazard and risk analyses rely on the simplistic infinite slope method to capture all modes of mass wasting. However, unique modes of mass wasting cause distinct consequences to the human environment (Pollock et al., 2019a). Slow-moving landslides tend to impact static infrastructure, especially extensive transportation networks, while rapid, localized flows pose greater risk to human lives. General infinite slope assumptions miss the nuanced consequences of unique movement modes (Hungr et al., 2014).

This research adopts the Multimodal Model developed and modified by A. Grant et al. (2016), Pollock et al. (2019a), Pollock & Wartman (2025).

4.1. Methodology

The Multimodal physics-based model MM_3 (Pollock & Wartman, 2025) was initially created for risk assessment, understanding risk as a combination of hazard, susceptibility, and vulnerability. It adopts the pixel-based, multimodal co-seismic landslide hazard method of A. Grant et al. (2016) and presents a parallel set of mode-specific models for rainfall-induced landslides. Simple, physics-based models are used to calculate the factor of safety (FS) against shallow, disrupted slides; rockfall; and rotational, coherent slumps. The model for co-seismic rotational slumps was expanded to three dimensions.

However, this study implements a slight simplification in the co-seismic initiation hazard to enable comparisons between the updated inventory (reality) and MM_3 simulation. Specifically, rockfall and debris slide modes are now modeled as infinite slope (Duncan, 2014), and rotational slumps are modeled using the rotational slump approach from Pollock et al. (2019).

The MM_3 workflow is described in Figure 14. After calculating the factor of safety for different modes using Equation 3, a Simplified Newmark Analysis calculates the critical yield acceleration (Ky) using Equation 4 following Chien & Tsai (2017). With Ky and PGA from Bradley et al., (2017), an empirical correlation is used to determine co-seismic displacement following Saygili & Rathje (2008) in Equation 5.

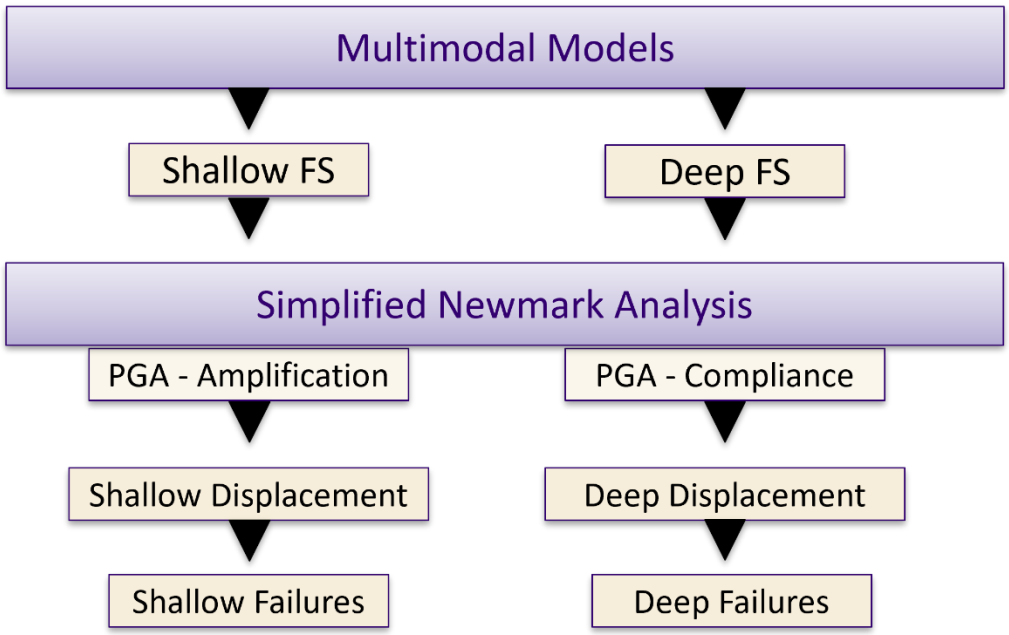

Figure 14. Workflow of MM_3 co-seismic hazard initiation model.

Then, MM_3 needs a displacement threshold from which it will determine pixels that fail and pixels that do not fail. The final step of this workflow consists in running 'n' Monte Carlo simulations, that account for variability in input parameters like strength: cohesion and friction angle, to finally find the probability of failure as the average the 'n' outputs. Sections 4.1.1 and 4.1.2 emphasize the formulations for calculating probability of failure for both shallow and deep landslides.

4.1.1. Shallow Model

The static factor of safety against shallow, planar slides is calculated with the classic infinite slope equation, modified to include the effects of root cohesion as follows in Equation 3 (Duncan et al., 2014) and the geometry is shown in Figure 15 after (Baum et al., 2008).

$$FS = \frac{(c + c_r) + (\gamma z \cos^2 \beta - \mu) \tan \varphi}{\gamma z \cos \beta \sin \beta} \qquad \textit{Equation 3}$$

Where FS is the factor of safety, c is cohesion, cr is root cohesion [kPa], γ is unit weight of the soil [kN/m³], β is the slope angle [rad], φ is the friction angle [rad], and u is the pore pressure acting on the failure plane, $u = \gamma w\ (z - zw)$. γw is the unit weight of water [kN/m³].

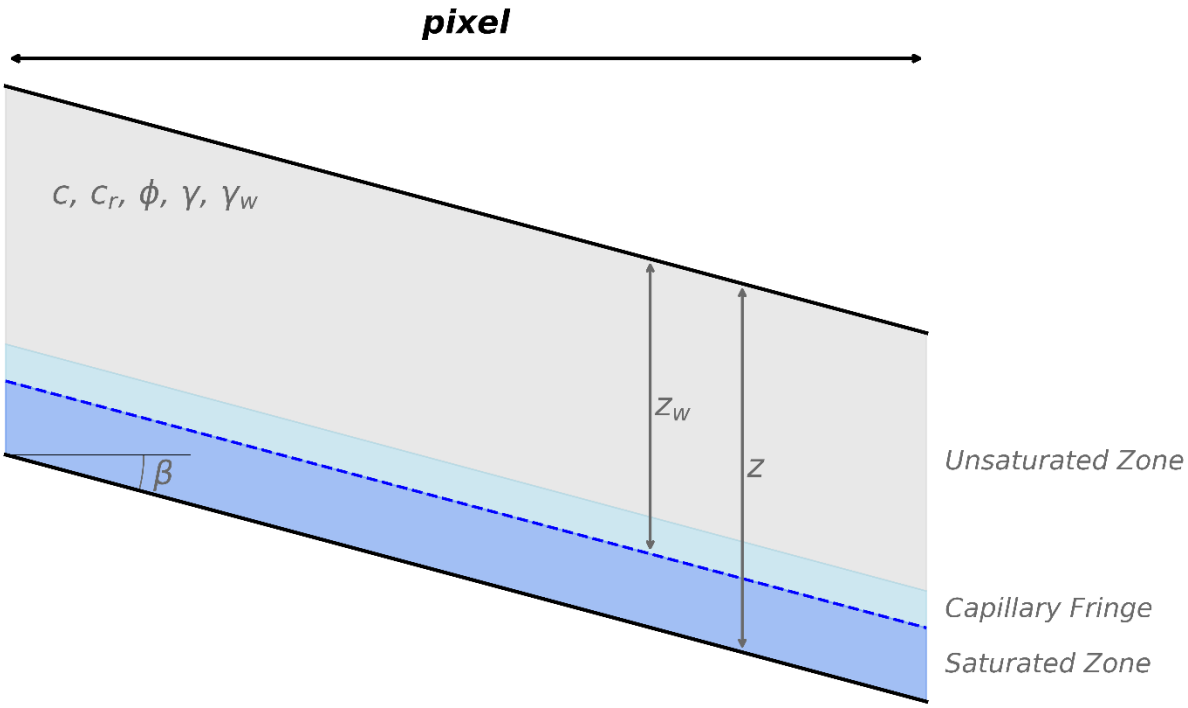

Figure 15. Illustration of infinite slope model for FS calculations in the shallow model.

Static factors of safety are converted to yield accelerations using the adapted Newmark equation of (Chien & Tsai, 2017) expressed in Equation 4. Finally, co-seismic displacements, Dn [cm], are estimated from PGA after (Rathje & Saygili, 2009) in Equation 5. Note that one of the improvements incorporated in this study is that now, the topographic amplification factors from (Massey CI et al., 2023) are included in the calculations.

$$k_y = \frac{FS\ - 1}{\frac{1}{tan\,\varphi} + tan\,\beta} \qquad \textit{Equation 4}$$

$$ln\,D_n = 5.52\ - 4.43\left(\frac{ky}{PGA\ *\ TAF}\right) - 20.93\left(\frac{ky}{PGA\ *\ TAF}\right)^2 + 42.61\left(\frac{ky}{PGA\ *\ TAF}\right)^3 - 28.74\left(\frac{ky}{PGA\ *\ TAF}\right)^4 + 0.72\,ln(PGA\ *\ TAF) \qquad \textit{Equation 5}$$

4.1.2. Deep model

Pollock et al., (2019b) develop an efficient, three-dimensional, pixel-based rotational failure model that computes the limit-equilibrium FS for a uniform, idealized failure surface that combines larger hillslope conditions with individual pixel properties, such as cohesion and friction angle (Figure 16). The efficiency of the model comes from the limiting assumption of a single prescribed failure surface. The location of the critical failure surface, defined by a depth parameter, p, is determined graphically (Pollock & Wartman, 2025). The static factor of safety is then calculated using the Equation 6

$$FS = \frac{2\pi Rbc\ +\ (W\,cos\,\alpha - U)\,tan\,\varphi}{W\,sin\,\alpha} \qquad \textit{Equation 6}$$

Where c and φ are the cohesion [kPa] and friction angle [rad] of the soil mass, and α is the basal angle [rad] given by Equation 7. The weight of the sliding block, W, is given by Equation 8 (b is computed from Equation 9). The radius of failure is a function of local relief

calculated from Equation 10. The resultant force of the pore water pressure is calculated from Equation 11.

$$\alpha = sin^{-1}\frac{4\,sin\,\theta\,(sin\,\delta)^3}{3(2\delta - sin\,2\delta)} \qquad \textit{Equation 7}$$

$$W = \frac{\pi\gamma b^2}{3}(3R - b) \qquad \textit{Equation 8}$$

$$b = R(1 - cos\,\delta) \qquad \textit{Equation 9}$$

$$R = \frac{H}{4}\left(\frac{cos\,\beta}{p(sin\,\beta)^2} + \frac{p}{cos\,\beta}\right) \qquad \textit{Equation 10}$$

$$U = \frac{\pi\gamma_w q^2}{3}(3R - q) \qquad \textit{Equation 11}$$

Where H is local hillslope relief [m] and p is the depth parameter. The internal angle, δ, is computed as $\delta = sin^{-1}\frac{H}{2R\,sin\,\beta}$ [rad] for slopes 10◦≤ β≤ 35◦, θ is determined by the water table depth, and $q = R(1 - cos\,\theta)$.

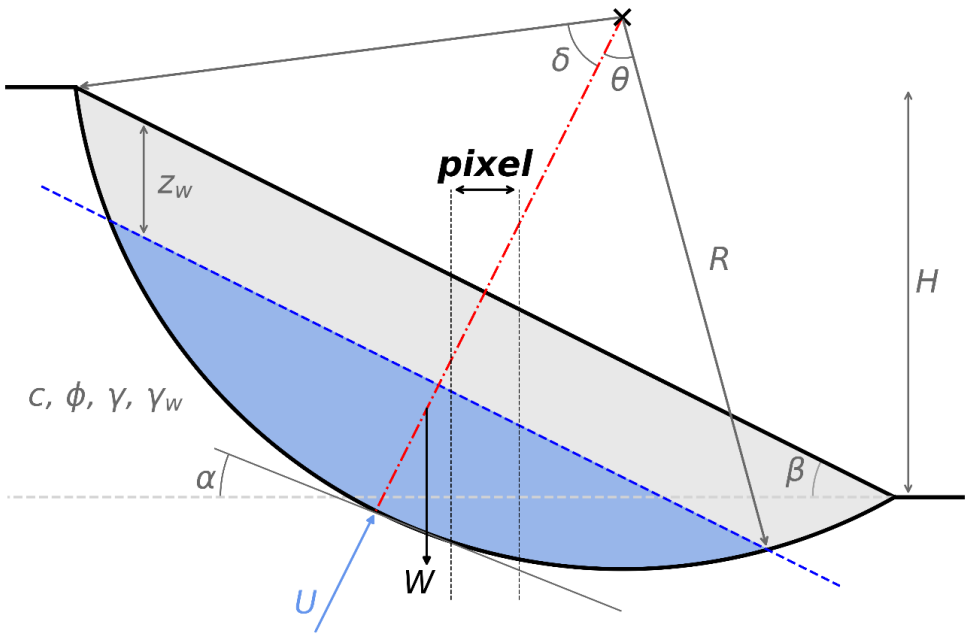

Figure 16. Illustration of Bishop rotational slump model for FS calculations in the deep model.

Similarly, as in the shallow model, static factors of safety are converted to yield accelerations using the adapted Newmark equation of (Chien & Tsai, 2017) expressed in Equation 4. Finally, co-seismic displacements, Dn [cm], are estimated from PGA after (Rathje & Saygili, 2009) in Equation 11. Note that a compliance factor, C, is included in the calculations for deep slides, and the reasoning or this is that this model accounts reductions in ground motions due to incoherence within the big mass during an earthquake.

$$\ln D_n = 5.52 - 4.43\left(\frac{ky}{PGA * TAF * C}\right) - 20.93\left(\frac{ky}{PGA * TAF * C}\right)^2 + 42.61\left(\frac{ky}{PGA * TAF * C}\right)^3 - 28.74\left(\frac{ky}{PGA * TAF * C}\right)^4 + 0.72\ln(PGA * TAF * C) \quad \textit{Equation 12}$$

4.2. Sensitivity Analysis

A tornado diagram-based sensitivity analysis was performed to identify which input variables the MM_3 model is most sensitive to. In this type of analysis, variables are ranked by their influence on the model output, with the most influential variable placed at the top of the chart and others listed in descending order of impact. Each variable's range of influence is represented as a horizontal bar, with units tailored to the context (e.g., percentage change, time, or cost). This visual format facilitates rapid identification of the parameters that exert the strongest control over the model's behavior. Tornado diagrams are well suited for evaluating the sensitivity of models to multiple parameters and are commonly used for their interpretability (Eschenbach, 1992). In this study, the dependent variable was the predicted susceptible area to earthquake-induced landslides in square kilometers (km^2).

The baseline, lower, and upper bounds for the model parameters used in this sensitivity analysis are summarized in Table 2. These bounds were carefully selected to reflect the expected range of variability for each parameter, drawing on domain expertise as well as empirical and model-derived data. For most geotechnical parameters, such as cohesion, friction angle (ϕ), soil depth, dry unit weight, Newmark displacement, local relief, and compliance, the ranges were established through expert judgment, informed by typical values observed both within the study area and in broader geotechnical literature. This approach was necessary given the lack of spatially continuous field measurements or detailed statistical distributions for these variables.

Table 2. Summary of bounds in input parameters for sensitivity analysis.

Variable	Mode					
	Shallow			Deep		
	Lower Bound	Baseline	Upper Bound	Lower Bound	Baseline	Upper Bound
TAF	1	1.4	1.6	1	1.4	1.6
Dry unit weight (kN/m³)	16.5	18	19	16.5	18	19
Soild Depth (m)	1	5	8	-	-	-
Newmark Displacement (m)	2	5	20	2	5	20
Local Relief (m)	150	300	400	150	300	400
Compliance	-	-	-	0.2	0.5	1
PGA (g)	0.2	0.4	0.9	0.2	0.4	0.9
Phi Greywacke - Cretaceous (°)	31	38	45	31	38	45
Phi Siltstones - Neogene (°)	15	24	28	15	24	28
Cohesion Greywacke - Cretaceous (kPa)	5	18	20	5	18	20
Cohesion Siltstones - Neogene (kPa)	15	21	35	15	21	35

In contrast, parameters like the topographic amplification factor (TAF) and peak ground acceleration (PGA) were bounded using empirical and modeling data. The TAF bounds were informed by the spatial variation reported by Massey et al. (2023), who characterized seismic shaking amplification across diverse terrain types in New Zealand. Meanwhile, the PGA bounds were derived from the spatial variability predicted by the (Bradley et al., 2017) ground motion model during the Kaikoura earthquake. Incorporating these data-driven constraints ensured that the sensitivity analysis remained grounded in physically plausible scenarios and accurately reflected observed and modeled seismic behavior during the triggering event.

All selected variables serve either as direct inputs to the MM_3 landslide susceptibility model or as fixed assumptions within its internal framework. To quantify the influence of each parameter on the predicted susceptible area, a tornado diagram-based sensitivity analysis was employed. The results, depicted in Figure 17, express changes as percentages relative to the baseline area identified as susceptible to failure. The baseline predicted susceptible area was approximately 15 km² for shallow landslides and 7.19 km² for deep-seated landslides. These baseline values provide an essential reference for interpreting the variations shown in the tornado diagrams in Figure 17.

In the shallow model, varying the PGA across its bounds produced the most substantial change, with the upper bound increasing the susceptible area by nearly 130% (from 15 km² to approximately 34 km²) and the lower bound reducing it by nearly 50%, essentially eliminating predicted shallow failures under weak shaking scenarios. Similarly, soil depth showed a striking influence, where deeper assumed layers led to a ~45% increase (up to 23 km²), while reducing depth sharply decreased susceptibility.

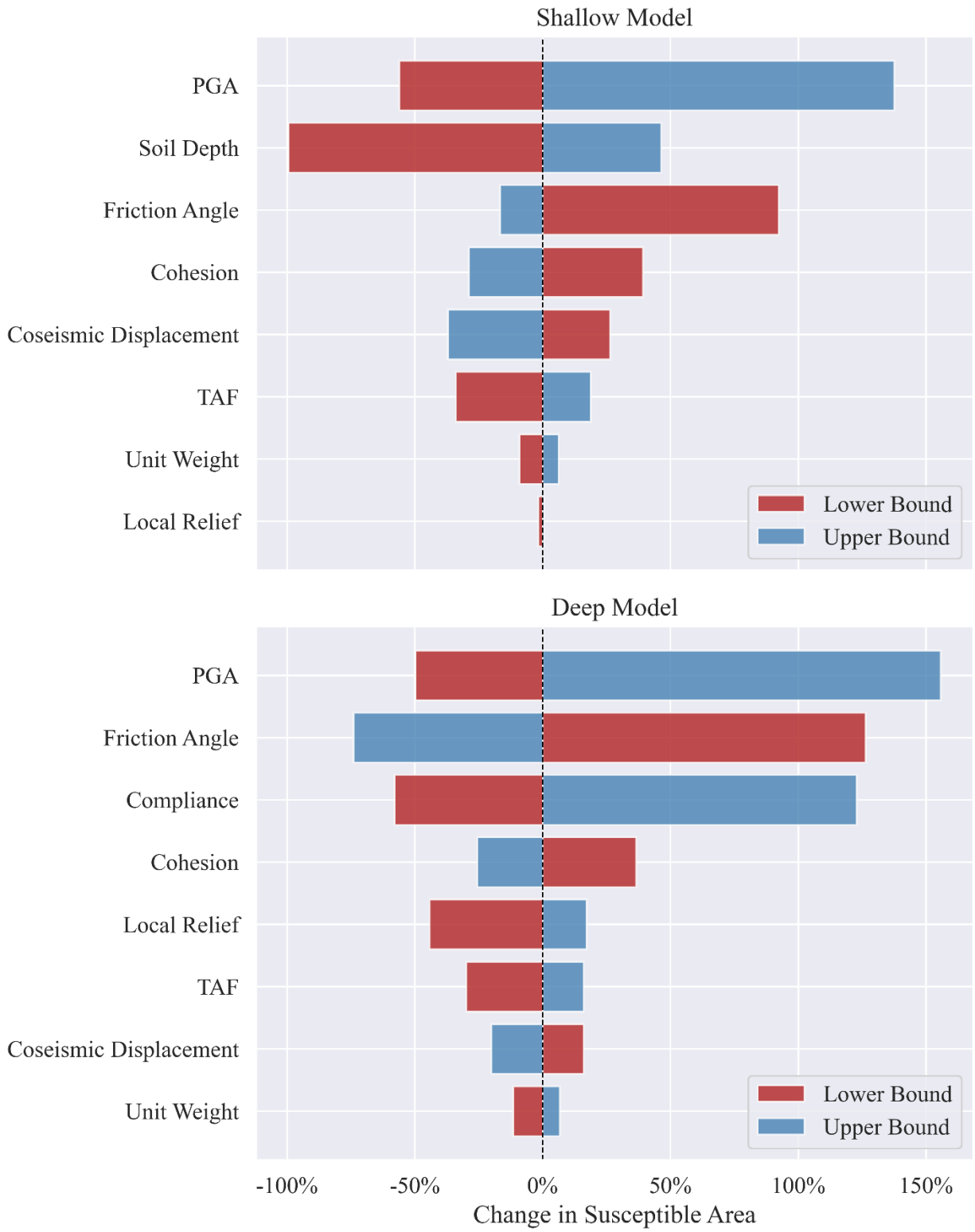

Figure 17. Results of the sensitivity analysis, performed in both shallow and deep model.

Changes in friction angle and cohesion also significantly impacted the results. For example, the lower bound of friction angle led to a ~80% increase, expanding the predicted susceptible area to ~27 km², while a higher friction angle cut it by over 60%, down to ~6 km². Cohesion exhibited a symmetrical but milder pattern, varying the susceptible area from approximately 7 to 21 km² depending on strength assumptions. Secondary influences included coseismic displacement, TAF, and local relief, each contributing moderate shifts, while unit weight showed a minimal effect, varying total susceptible area by less than 10% in either direction.

In the deep-seated model, PGA remained the most influential factor, with the upper bound pushing susceptibility to over 18 km², a 150% increase from the baseline, and the lower bound reducing it to nearly zero. Friction angle and compliance closely followed, each capable of more than doubling or halving the predicted area depending on their values. Notably, compliance's influence reiterates that slope deformability significantly modulates how ground shaking translates into failure potential, reinforcing the model's seismic sensitivity. The response to cohesion and local relief was also substantial, with changes in either parameter leading to susceptible area estimates ranging between ~3 and 12 km². TAF and coseismic displacement produced moderate impacts, while unit weight again showed only minor variation.

The analysis clearly indicates that the MM_3 model is particularly sensitive to variations in PGA, friction angle, and cohesion, with these parameters strongly influencing susceptibility predictions for both shallow and deep-seated landslides. Notably, PGA exhibited the most pronounced effect, consistent with the understanding that seismic shaking intensity is the primary driver of earthquake-induced slope failures. Sensitivity to shear strength variations was also pronounced, particularly in geologic units such as Neogene siltstones and Cretaceous

greywackes, which together represent more than 70% of the study area. For shallow landslides, soil depth emerged as another critical factor, with deeper soil layers substantially increasing the predicted susceptible area. This highlights the importance of accurately characterizing colluvial soil deposits, the depth of weathered zones (regolith soils), and the nature of the parental rocks from which these soils are derived when assessing shallow landslide hazards, as these factors collectively influence the strength, permeability, and failure behavior of near-surface materials.

While PGA and shear strength parameters remained dominant, secondary factors including local relief, Newmark displacement, and TAF contributed measurable effects. Conversely, dry unit weight exerted a comparatively minor influence on model outputs in both failure modes. These nuanced findings are all detailed in Figure 17.

An additional refinement involved applying slope masking thresholds to spatially constrain susceptibility predictions to topographic zones consistent with observed landslide occurrence. Analysis of the updated landslide inventory revealed that shallow landslides preferentially occur on slopes between 40° and 50°, whereas deep-seated landslides tend to cluster on gentler slopes ranging from 20° to 30°. To incorporate these empirical observations, the shallow model was limited to slopes between 15° and 90°, while the deep model was constrained to slopes between 5° and 65°. These thresholds differ modestly from MM_3's original classification, rock falls (35°–90°), shallow debris slides (15°–50°), and soil or rock slumps (10°–35°), representing a pragmatic adjustment grounded in observed behavior and supported by multiple simulation outputs of the model, rather than purely theoretical assumptions.

In summary, these quantified sensitivities, grounded in both percentage and absolute area terms, reinforce that PGA, shear strength parameters, and soil characteristics are the dominant controls on earthquake-induced landslide susceptibility. Moreover, they illustrate not only how

critical it is to properly constrain these variables, but also how essential it is to prioritize future research efforts aimed at refining model representations and reducing uncertainty in key geotechnical and seismic inputs. This is particularly crucial for the MM_3 framework, which is highly responsive to variability in these parameters. Enhancing the spatial resolution and reliability of such inputs, through targeted field investigations, advanced remote sensing, and systematic geotechnical testing, will directly improve MM_3's predictive performance and the overall robustness of landslide susceptibility assessments in seismically active terrain.

4.3. Validation

Model validation is a critical step in evaluating the accuracy and reliability of landslide susceptibility models. MM_3 validation was conducted using the Area Under the Curve (AUC) of the Receiver Operating Characteristics (ROC) curve, a technique for visualizing, organizing, and selecting classifiers based on their performance (Fawcett, 2006). A discrete classifier applied to a test set generates two important statistics: the True Positive Rate (TPR, also called recall or sensitivity) and the False Positive Rate (FPR, also called false alarm rate) (Fawcett, 2008). Mathematical expressions for calculating TPR and FPR follow Equations 13 and 14, respectively. True positives, true negatives, false positives, and false negatives are described in the confusion matrix in Table 3.

$$TPR = \frac{Positives\ correctly\ classified}{Total\ Positives} = \frac{TP}{TP + FN} \qquad \textit{Equation 13}$$

$$FPR = \frac{Negatives\ incorrectly\ classified}{Total\ Negatives} = \frac{FP}{FP + TN} \qquad \textit{Equation 14}$$

Table 3. Confusion matrix after Fawcett, 2008

	Predicted Positive	**Predicted Negative**
Actual Positive	True Positive (TP)	False Negative (FN)
Actual Negative	False Positive (FP)	True Negative (TN)

The AUC of a classifier is equivalent to the probability that the classifier will rank a randomly chosen positive instance higher than a randomly chosen negative instance (Fawcett, 2008).

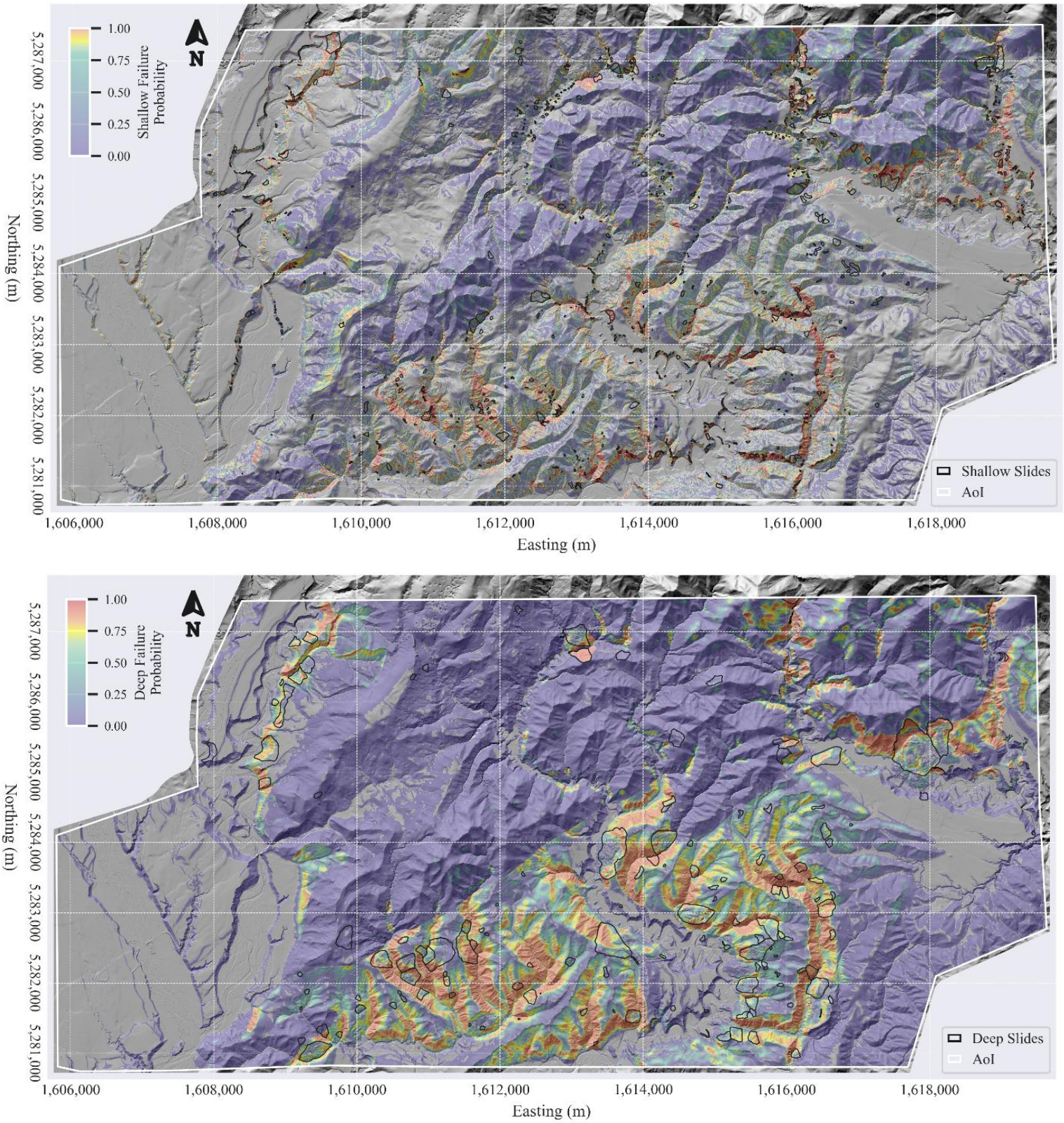

Figure 18. Probability of failure output maps from MM_3 for shallow slides on top and deep slides on the bottom.

Figure 18 presents the final susceptibility maps in terms of probability of failure generated with the MM_3 model for both failure modes: shallow landslides are displayed at the top, and deep-seated landslides at the bottom. The shallow model appears to capture more localized and finer-scale patterns of susceptibility, likely due to the influence of surface conditions such as slope angle, vegetation, and soil properties. In contrast, the deep-seated model outlines broader zones of elevated risk, which may reflect the importance of structural and lithological controls at greater depths.

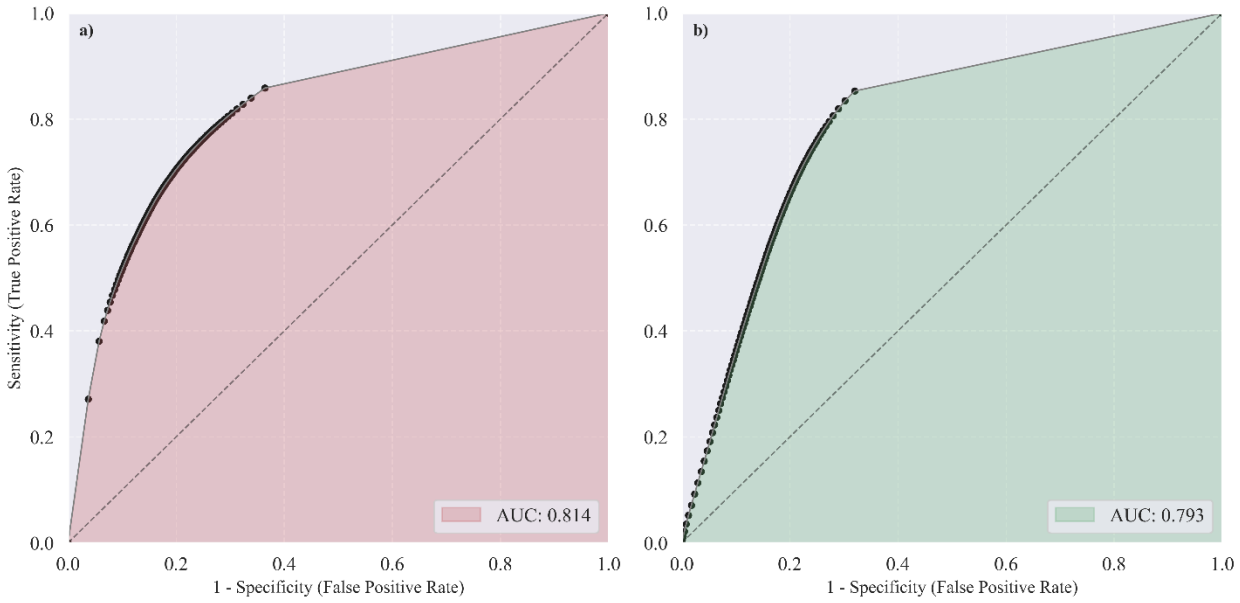

Figure 19. ROC curves with AUC values for both a) shallow (red) and b) deep (green) slides.

Figure 19 summarizes the overall performance of both models using the AUC metric. The shallow landslide model achieves an AUC of 0.814 (shown in red), indicating strong predictive capability. The deep-seated landslide model, with an AUC of 0.793 (shown in green), also demonstrates good predictive performance, though slightly lower than the shallow model. This difference may stem from the more complex and less well-constrained nature of deep-seated

failures, which often involve subsurface processes that are not directly observable or easily quantified.

Importantly, both models initially produced AUC values near 0.6, reflecting relatively weak predictive skill in early configurations. Through systematic variation of the geotechnical and morphological parameters summarized in Table 2, including cohesion, friction angle (ϕ), soil depth, dry unit weight, Newmark displacement, local relief, and compliance.

An extensive sensitivity exploration of over 25,000 simulations was conducted. This allowed for the identification of parameter combinations that substantially improved the model performance. It is important to note that PGA and TAF were not varied during this process, as their values were directly adopted from Bradley et al. (2017) and Massey et al. (2023) and were thus geographically referenced to preserve physical realism. The resulting improvement in AUC underscores the importance of careful model calibration and parameter sensitivity analysis. It also highlights how targeted refinement of uncertain inputs can enhance the ability of susceptibility models to replicate observed landslide patterns in complex terrain.

Figure 20 presents the combined landslide susceptibility map, which integrates the outputs of both the shallow and deep-seated failure mechanisms from MM_3 model into a unified spatial classification. The map uses a four-color scheme to distinguish between areas with no susceptibility (gray), exclusive susceptibility to shallow failures (red), susceptibility to deep-seated failures only (green), and zones where both failure mechanisms are predicted to occur (orange). In addition, black outlines mark landslides from the mapped inventory, providing spatial validation against observed events.

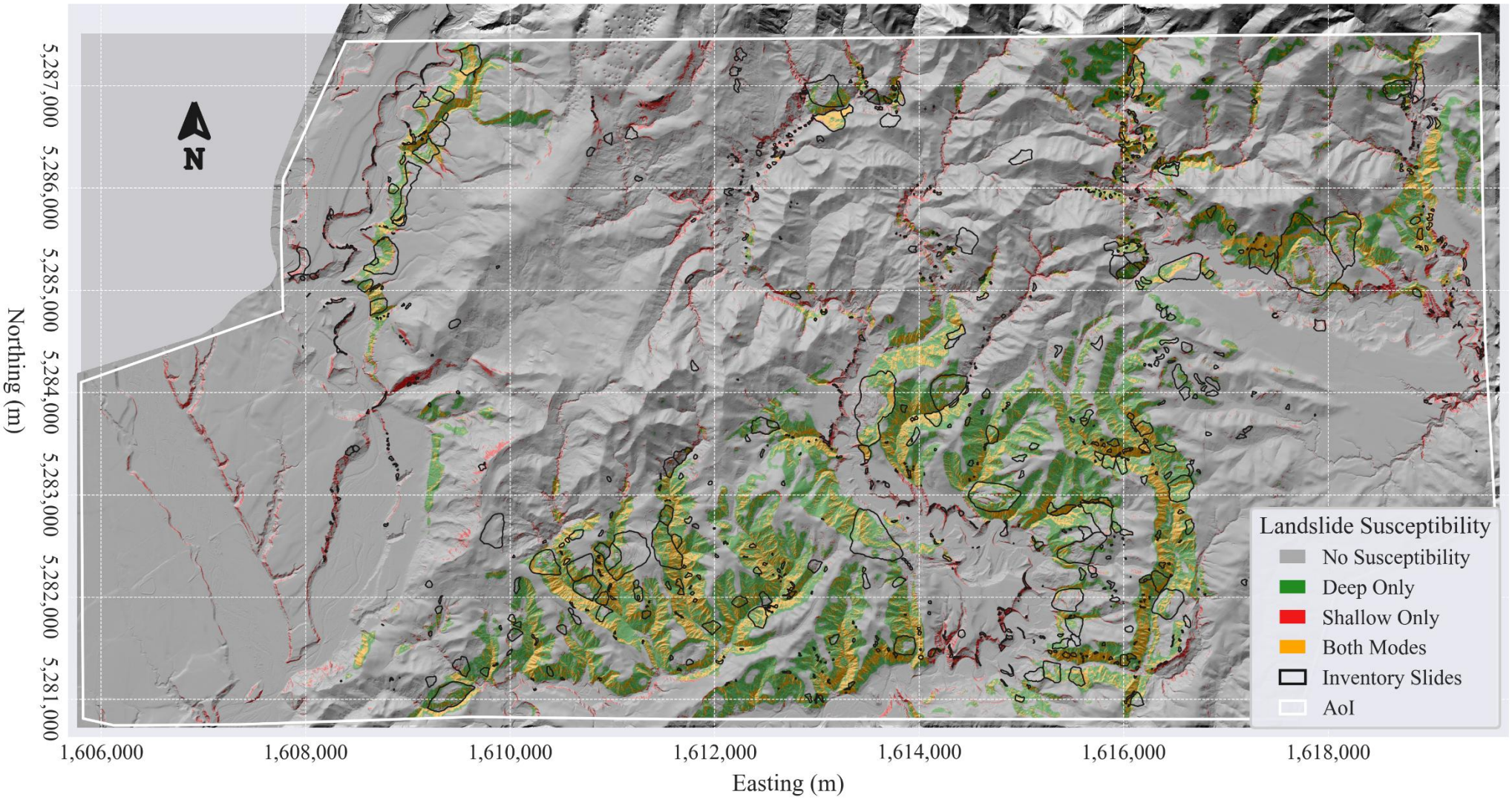

Figure 20. Combined susceptibility map for the study area.

The spatial distribution of susceptibility classes closely reflects terrain morphology and failure mode behavior. Susceptible areas, colored red, green, or orange, are predominantly located on steep hillslopes, valley flanks, and ridge lines, while non-susceptible areas are generally associated with flatter interfluves and depositional terrain. The clustering of shallow susceptibility in steeper terrain with thin soil layers suggests gravitational and seismic forces dominate in these zones, rapidly triggering shallow slides. Conversely, deep-seated failures tend to occur in terrain underlain by thick regolith, weathered bedrock, or tectonically weakened materials, where failures initiate at depth and involve more complex deformation patterns.

The orange areas, representing combined susceptibility, are of particular importance. These zones reflect the convergence of physical conditions favoring both failure modes and may be indicative of slope systems with deeply weathered profiles with loose, shallow soils, conditions under which both shallow surficial failures and deeper-seated mass movements could be both triggered during seismic events. These areas pose the greatest susceptibility and should be prioritized in future monitoring, land-use planning, and hazard mitigation efforts.

The performance of the underlying models, summarized in Figure 19, provides context for interpreting the combined output. The differences in predictive performance further justify the multimodal structure of the MM_3 framework, in which each failure mode is modeled independently based on distinct physical controls.

The overlay of the observed landslide inventory supports the overall accuracy of the classification, with a significant proportion of known landslides falling within predicted susceptible areas, particularly in the red and orange zones, indicating strong spatial alignment between model outputs and actual failure locations. However, instances where mapped landslides lie outside predicted zones may reflect limitations in input data resolution, localized anomalies,

or failures triggered by processes not explicitly captured in the current modeling framework. These mismatches may also highlight the absence of critical conditioning variables, such as spatial variability in soil depth, subsurface structures like bedding orientation, fault zones, or stratigraphic discontinuities, which are challenging to map and model but play a pivotal role in slope failure. While the MM_3 model already captures a substantial portion of observed variability, especially for shallow failures, its performance could be further enhanced through the incorporation of high-resolution subsurface data, targeted geotechnical field investigations, and time-dependent triggering thresholds, particularly for improving the prediction of deep-seated landslides.

In conclusion, the combined susceptibility map (Figure 20) exemplifies the value of a multimodal, empirically constrained approach to landslide susceptibility modeling. By distinguishing shallow and deep-seated failure potential, and mapping where these may overlap, the output provides critical insights for understanding and managing landslide hazards in seismically active, mountainous terrain. Coupled with the robust model performance shown in Figure 19, these results affirm both the methodological soundness and practical relevance of the MM_3 framework for earthquake-induced landslide susceptibility assessment.

5. Discussion

The comparative analysis of the shallow and deep landslide models reveals that, despite achieving good predictive performance, with an AUC of 0.814 for the shallow model and 0.793 for the deep model, there is still significant potential for improvement.

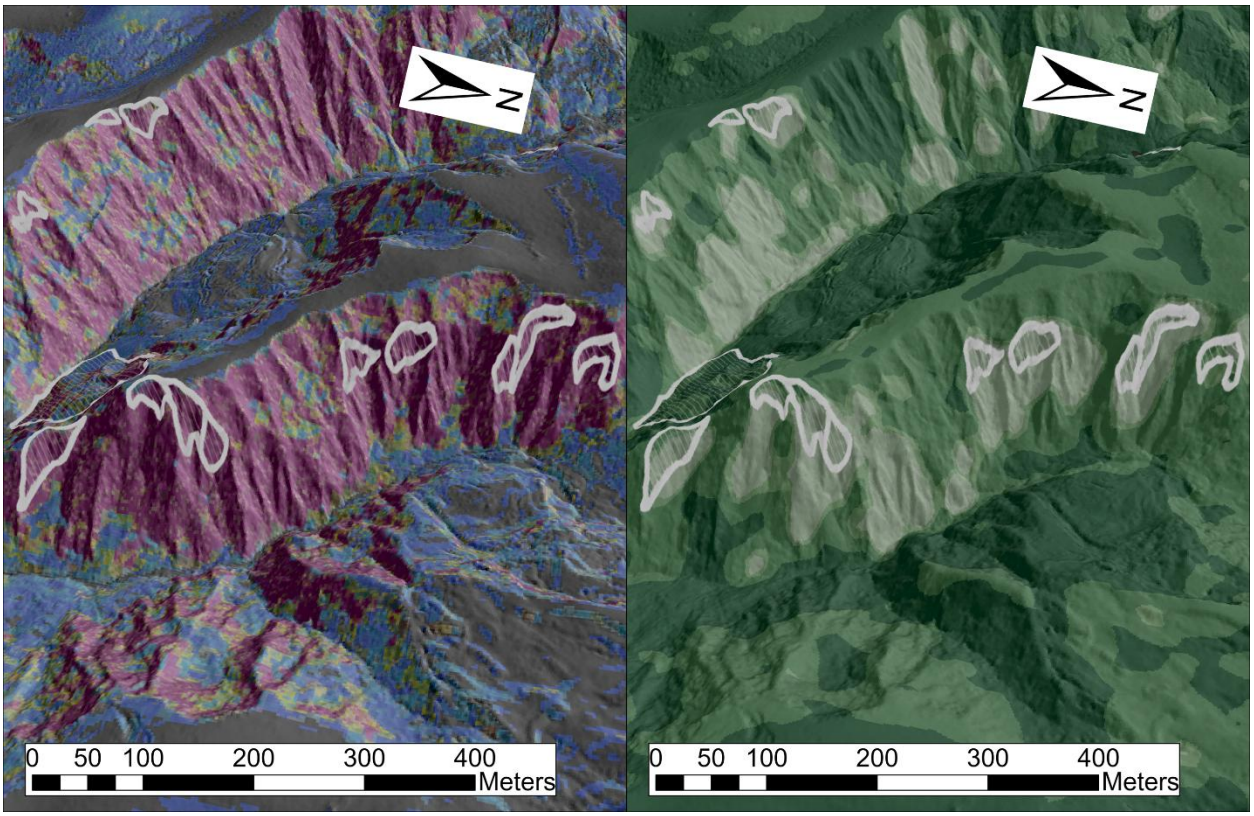

Figure 21. Shallow model outputs and improvement opportunities.

For shallow failures, the model currently tends to overpredict landslides in regions with steeper slopes, even though the geospatial data analysis indicates that other factors, such as vegetation cover (NDVI), are also critical. At present, the influence of NDVI in the model is limited, which means the stabilizing effects of vegetation, particularly its contribution through root cohesion, does not highlight in the outputs (see Figure 21). Enhancing the sensitivity of NDVI within the model could help to refine predictions by better representing the role of vegetation in mitigating landslide risk. Moreover, the variability in soil depth is also a significant

factor in shallow landslide susceptibility. The sensitivity analysis shows that shallow failures are highly dependent on soil thickness, yet the model does not currently incorporate detailed spatial variations in soil depth. Implementing a dedicated soil depth model would reduce uncertainty and improve the reliability of predictions for shallow failure zones.

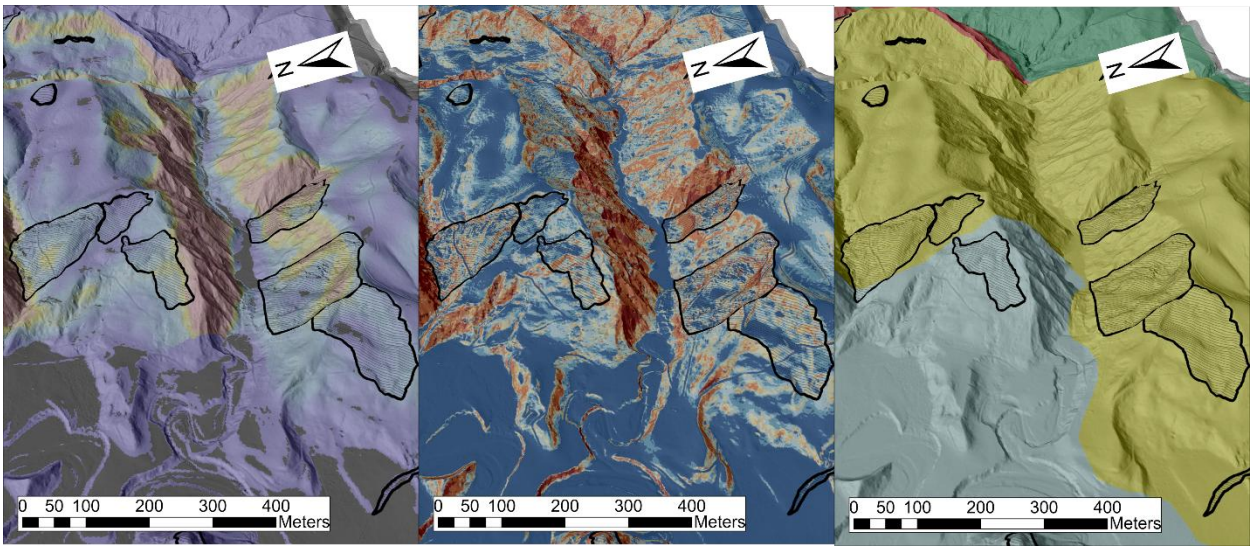

Figure 22. Deep model outputs and improvement opportunities.

For deep-seated landslides, while slope remains the dominant influencing factor, the model exhibits a dual limitation: it overpredicts landslides in steeper areas but underpredicts them on less steep slopes (see Figure 22). This discrepancy likely arises because deep failures are not strongly governed by slope angle. Currently, the absence of geological features as preferential planes for failure (e.g., bedding or stratification) in the model leads to underprediction in areas where such preferential planes exist. Incorporating variables that account for bedding, stratification, and other structural discontinuities would likely enhance the accuracy of the deep landslide predictions.

In summary, while MM_3 models currently perform well as indicated by their respective AUC values, there remains room for refinement. By increasing the model sensitivity to NDVI

and integrating more detailed soil depth information for shallow failures, and by including structural geological controls for deep-seated landslides, the overall predictive capability of both models can be further improved. These enhancements would enable a more nuanced capture of the complex processes governing landslide occurrence and ultimately contribute to more effective hazard assessment.

6. Conclusions

The analysis of the high-resolution inventory provided valuable insights into the factors governing earthquake-induced landslides. In particular, the statistical analysis using the frequency ratio method revealed that the topographic amplification factor (TAF), slope, geology, and normalized difference vegetation index (NDVI) are strongly correlated with landslide occurrences. These correlations establish a robust basis for integrating diverse geomorphic and environmental variables into hazard assessments.

Building upon these statistical findings, the sensitivity analysis of the Multimodal Physics-Based Model (MM_3) further clarified the influential factors affecting landslide probability. Specifically, the analysis showed that peak ground acceleration (PGA), friction angle, and cohesion are the most critical variables for determining the occurrence of earthquake-induced landslides. Additionally, for shallow failures, the model exhibited a high sensitivity to soil depth. This complementary insight underscores the need to incorporate detailed soil characteristics and dynamic ground motion parameters to better capture the complexities of landslide initiation.

Integrating these layers of analysis, MM_3 was rigorously tested against a high-resolution landslide inventory. The validation process yielded good performance metrics, with the model

achieving a global accuracy reflected in AUC values of 0.814 for shallow landslides and 0.793 for deep landslides. Notably, attaining these high AUC scores required the execution of over 25,000 simulations, during which input parameters were systematically varied until the optimal set of configurations emerged. This exhaustive simulation process highlights both the robustness of MM_3 and the level of calibration required to accurately reflect complex real-world behavior.

In summary, this study demonstrates that while MM_3 already performs well, there is significant potential for further improvements. The strong correlations revealed by frequency ratio analysis, combined with the critical sensitivities identified in the model, suggest that refining NDVI effects, soil depth inputs, and incorporating additional structural geological controls (such as bedding and foliation for deep-seated failures) could enhance predictive accuracy even further. These enhancements can pave the way for more effective early warning systems and risk mitigation strategies in seismically active, landslide-prone regions.

7. References

Baum, R. L., Savage, W. Z., & Godt, J. W. (2008). *TRIGRS-A Fortran Program for Transient Rainfall Infiltration and Grid-Based Regional Slope-Stability Analysis, Version 2.0*. http://geohazards.cr.usgs.gov/

Bradley, B. A., Razafindrakoto, H. N. T., & Polak, V. (2017). Ground-motion observations from the 14 November 2016 Mw 7.8 Kaikoura, New Zealand, earthquake and insights from broadband simulations. *Seismological Research Letters*, *88*(3), 740–756. https://doi.org/10.1785/0220160225

Chien, Y.-C., & Tsai, C.-C. (2017). Immediate Estimation of Yield Acceleration for Shallow and Deep Failures in Slope-Stability Analyses. *International Journal of Geomechanics*, *17*(7). https://doi.org/10.1061/(ASCE)GM.1943-5622.0000884

Dahal, A., Castro-Cruz, D. A., Tanyaş, H., Fadel, I., Mai, P. M., van der Meijde, M., van Westen, C., Huser, R., & Lombardo, L. (2023). From ground motion simulations to landslide occurrence prediction. *Geomorphology*, *441*, 108898. https://doi.org/10.1016/J.GEOMORPH.2023.108898

Dessington, R. S. (2020). *"Breaking New Ground"; An investigation into coseismic ground cracking following the 2016 Mw7.8 earthquake near Kaikoura, New Zealand*. Durham University.

Duncan, J., Wright, S., Brandon, T., & 2014. (2014). *Soil Strength and Slope Stability*. Hoboken: John Wiley & Sons.

Eschenbach, T. G. (1992). Spiderplots versus Tornado Diagrams for Sensitivity Analysis. *Interfaces*, *22*(6), 40–46. https://doi.org/10.1287/inte.22.6.40

Fawcett, T. (2006). An introduction to ROC analysis. *Pattern Recognition Letters*, *27*(8), 861–874. https://doi.org/10.1016/J.PATREC.2005.10.010

Fawcett, T. (2008). PRIE: A system for generating rulelists to maximize ROC performance. *Data Mining and Knowledge Discovery*, *17*(2), 207–224. https://doi.org/10.1007/s10618-008-0089-y

Grant, A. R. R., & Culhane, N. K. (2025). Global Patterns of coseismic landslide runout mobility differ from aseismic landslide trends. *Engineering Geology*, *344*. https://doi.org/10.1016/j.enggeo.2024.107824

Grant, A., Wartman, J., & Abou-Jaoude, G. (2016). Multimodal method for coseismic landslide hazard assessment. *Engineering Geology*, *212*, 146–160. https://doi.org/10.1016/j.enggeo.2016.08.005

GUZZETTI, F., CARDINALI, M., & REICHENBACH, P. (1996). The Influence of Structural Setting and Lithology on Landslide Type and Pattern. *Environmental & Engineering Geoscience*, *II*(4), 531–555. https://doi.org/10.2113/gseegeosci.II.4.531

Guzzetti, F., Malamud, B. D., Turcotte, D. L., & Reichenbach, P. (2002). Power-law correlations of landslide areas in central Italy. *Earth and Planetary Science Letters*, *195*(3–4), 169–183. https://doi.org/10.1016/S0012-821X(01)00589-1

Guzzetti, F., Mondini, A. C., Cardinali, M., Fiorucci, F., Santangelo, M., & Chang, K. T. (2012). Landslide inventory maps: New tools for an old problem. *Earth-Science Reviews*, *112*(1–2), 42–66. https://doi.org/10.1016/J.EARSCIREV.2012.02.001

Hungr, O., Leroueil, S., & Picarelli, L. (2014). The Varnes classification of landslide types, an update. In *Landslides* (Vol. 11, Issue 2, pp. 167–194). Springer Verlag. https://doi.org/10.1007/s10346-013-0436-y

Jaafari, A., Najafi, A., Pourghasemi, H. R., Rezaeian, J., & Sattarian, A. (2014). GIS-based frequency ratio and index of entropy models for landslide susceptibility assessment in the Caspian forest, northern Iran. *International Journal of Environmental Science and Technology*, *11*(4), 909–926. https://doi.org/10.1007/s13762-013-0464-0

Jasiewicz, J., & Stepinski, T. F. (2013). Geomorphons-a pattern recognition approach to classification and mapping of landforms. *Geomorphology*, *182*, 147–156. https://doi.org/10.1016/j.geomorph.2012.11.005

Jones, K. E., Howarth, J. D., Massey, C. I., Luković, B., Sirguey, P., Singeisen, C., Gasston, C., Morgenstern, R., & Ries, W. (2025). An alternative to landslide volume-area scaling relationships: an ensemble approach adopting a difference model to estimate the total

volume of landsliding triggered by the 2016 Kaikōura earthquake, New Zealand. *Landslides*, *22*(7), 2219–2236. https://doi.org/10.1007/s10346-025-02479-x

Kaiser, A., Balfour, N., Fry, B., Holden, C., Litchfield, N., Gerstenberger, M., D'Anastasio, E., Horspool, N., McVerry, G., Ristau, J., Bannister, S., Christophersen, A., Clark, K., Power, W., Rhoades, D., Massey, C., Hamling, I., Wallace, L., Mountjoy, J., … Gledhill, K. (2017). The 2016 Kaikōura, New Zealand, Earthquake: Preliminary Seismological Report. *Seismological Research Letters*, *88*(3), 727–739. https://doi.org/10.1785/0220170018

Kaiser, A., Massey, C., & Holden, C. (2014). *Site amplification, polarity and topographic effects in the Port Hills during the Canterbury earthquake sequence BIBLIOGRAPHIC REFERENCE*.

Kriegler, F. J., Malila, W. A., Nalepka, R. F., & Richardson, W. (1969). Preprocessing transformations and their effect on multispectral recognition. *International Symposium on Remote Sensing of Environment, University of Michigan, Ann Arbor, MI*, 97–131.

Langridge, R., Ries, W., Litchfield, N., Villamor, P., Van Dissen, R., Barrell, D., Rattenbury, M., Heron, D., Haubrock, S., Townsend, D., Lee, J., Berryman, K., Nicol, A., Cox, S., & Stirling, M. (2016). The New Zealand Active Faults Database. *New Zealand Journal of Geology and Geophysics*, *59*(1), 86–96. https://doi.org/10.1080/00288306.2015.1112818

Lee, S., & Min, K. (2001). Statistical analysis of landslide susceptibility at Yongin, Korea. *Environmental Geology*, *40*(9), 1095–1113. https://doi.org/10.1007/s002540100310

Lee, S., & Pradhan, B. (2007). Landslide hazard mapping at Selangor, Malaysia using frequency ratio and logistic regression models. *Landslides*, *4*(1), 33–41. https://doi.org/10.1007/s10346-006-0047-y

Lombardo, L., & Tanyas, H. (2022). From scenario-based seismic hazard to scenario-based landslide hazard: fast-forwarding to the future via statistical simulations. *Stochastic Environmental Research and Risk Assessment*, *36*(8), 2229–2242. https://doi.org/10.1007/s00477-021-02020-1

Massey, C., Townsend, D., Rathje, E., Allstadt, K. E., Lukovic, B., Kaneko, Y., Bradley, B., Wartman, J., Jibson, R. W., Petley, D. N., Horspool, N., Hamling, I., Carey, J., Cox, S.,

Davidson, J., Dellow, S., Godt, J. W., Holden, C., Jones, K., … Villeneuve, M. (2018). Landslides triggered by the 14 November 2016 Mw7.8 Kaikōura earthquake, New Zealand. *Bulletin of the Seismological Society of America*, *108*(3B), 1630–1648. https://doi.org/10.1785/0120170305

Massey CI, McColi ST, Lukovic B, Sadashiva VK, & Kaiser AE. (2023). *Development of Earthquake shaking vulnerability functions for residential buildings located on slopes in new zealand*.

Moore, J. R., Gischig, V., Burjanek, J., Loew, S., & Fäh, D. (2011). Site effects in unstable rock slopes: Dynamic behavior of the Randa instability (Switzerland). *Bulletin of the Seismological Society of America*, *101*(6), 3110–3116. https://doi.org/10.1785/0120110127

Pollock, W., Grant, A., Wartman, J., & Abou-Jaoude, G. (2019a). Multimodal method for landslide risk analysis. *MethodsX*, *6*, 827–836. https://doi.org/10.1016/j.mex.2019.04.012

Pollock, W., Grant, A., Wartman, J., & Abou-Jaoude, G. (2019b). Multimodal method for landslide risk analysis. *MethodsX*, *6*, 827–836. https://doi.org/10.1016/j.mex.2019.04.012

Pollock, W., & Wartman, J. (2025). MM_3: Multimodal framework for regional-scale quantitative landslide risk analysis. *MethodsX*, *14*, 103218. https://doi.org/10.1016/j.mex.2025.103218

Pollock, W., Wartman, J., Duvall, A., & Massey, C. (2020). *A framework for regional scale quantitative landslide risk analysis*. University of Washington.

Rathje, E. M., & Saygili, G. (2009). *Probabilistic assessment of earthquake-induced sliding displacements of natural slopes*.

Razavizadeh, S., Solaimani, K., Massironi, M., & Kavian, A. (2017). Mapping landslide susceptibility with frequency ratio, statistical index, and weights of evidence models: a case study in northern Iran. *Environmental Earth Sciences*, *76*(14). https://doi.org/10.1007/s12665-017-6839-7

Regmi, A. D., Devkota, K. C., Yoshida, K., Pradhan, B., Pourghasemi, H. R., Kumamoto, T., & Akgun, A. (2014). Application of frequency ratio, statistical index, and weights-of-evidence models and their comparison in landslide susceptibility mapping in Central Nepal

Himalaya. *Arabian Journal of Geosciences*, *7*(2), 725–742. https://doi.org/10.1007/s12517-012-0807-z

Saygili, G., & Rathje, E. M. (2008). Empirical Predictive Models for Earthquake-Induced Sliding Displacements of Slopes. *Journal of Geotechnical and Geoenvironmental Engineering*, *134*(6), 790–803. https://doi.org/10.1061/(ASCE)1090-0241(2008)134:6(790)

Stark, C. P., & Hovius, N. (2001). The characterization of landslide size distributions. *Geophysical Research Letters*, *28*(6), 1091–1094. https://doi.org/10.1029/2000GL008527

Tanyaş, H., Allstadt, K. E., & van Westen, C. J. (2018). An updated method for estimating landslide-event magnitude. *Earth Surface Processes and Landforms*, *43*(9), 1836–1847. https://doi.org/10.1002/esp.4359

van Westen, C. J., Castellanos, E., & Kuriakose, S. L. (2008). Spatial data for landslide susceptibility, hazard, and vulnerability assessment: An overview. *Engineering Geology*, *102*(3–4), 112–131. https://doi.org/10.1016/J.ENGGEO.2008.03.010